

A comparison of the excess mass around CFHTLenS galaxy-pairs to predictions from a semi-analytic model using galaxy-galaxy-galaxy lensing

P. Simon¹, H. Saghiha¹, S. Hilbert^{2,3}, P. Schneider¹, C. Boever¹

¹ Argelander-Institut für Astronomie, Universität Bonn, Auf dem Hügel 71, 53121 Bonn, Germany

² Exzellenzcluster Universe, Boltzmannstr. 2, 85748 Garching, Germany

³ Ludwig-Maximilians-Universität, Universitäts-Sternwarte, Scheinerstr. 1, 81679 München, Germany

Received / Accepted

ABSTRACT

The matter environment of galaxies is thought to be connected to the physics of galaxy formation and evolution. Especially the average matter distribution around galaxy pairs is a strong test for galaxy models. With galaxy-galaxy-galaxy lensing (G3L) as a probe we therefore map out the distribution of correlated excess-mass around galaxy pairs in the Canada-France-Hawaii Telescope Lensing Survey (CFHTLenS) in a reanalysis of the data. We compare the maps to predictions by a recent semi-analytic model (SAM) which is implanted on the Millennium Simulation. Our target galaxies span a range of stellar masses between $10^9 - 10^{11} M_{\odot}$ and have redshifts below $z \lesssim 0.6$ in two redshift bins; the projected separation between galaxies pairs is chosen between $\approx 170 - 300 h^{-1}$ kpc in two separation bins. Compared to an earlier G3L study with CFHTLenS galaxies, we make more efficient use of the data by performing the measurements on the four contiguous fields W1-W4 rather than individual pointings. In addition, we verify the accuracy of our refined stacking technique for the map construction with simulated data and provide a detailed description of the methodology. For a better interpretation of the maps, we discuss the impact of chance pairs, i.e., galaxy pairs that appear close to each other in projection only, and we introduce an alternative correlation map that is less affected by projection effects but has a lower signal-to-noise ratio (S/N). For all maps, we obtain significant measurements of the excess-mass distribution for all galaxy samples and an overall good agreement with the SAM predictions. There is, however, tentative evidence for a bulge-like feature in the distribution of excess mass that is not predicted by the SAM and similar models. Although we have no strong indications for systematic errors in the maps, this feature may be related to a residual B-mode pattern visible in the average of all maps. Alternatively, misaligned galaxy pairs inside matter halos or lensing by a misaligned distribution of the intra-cluster gas might also cause a bulge.

Key words. gravitational lensing: weak – large-scale structure of the Universe – cosmology: observations – galaxies: formation – galaxies: evolution – methods: numerical

1. Introduction

The standard model of cosmology assumes a statistically homogeneous and isotropic Universe in which the matter density is dominated by invisible, dissipationless cold dark matter; only a fraction of about 15 per cent is baryonic matter. Recent measurements strongly support a model with a spatially flat geometry and a lately accelerated expansion (e.g., Planck Collaboration et al. 2016, and references therein). In this picture, virialised halos of dark matter are assembled bottom-up over time by the gravitational collapse of initially small, adiabatic density fluctuations originating from the early Universe. Galaxies form inside the potential wells of matter halos from cooled, infalling baryonic gas with highest efficiency inside halos of virial mass $\sim 10^{12} M_{\odot}$ (see Mo et al. 2010 for a review). The conditions for galaxy formation are determined by the details of gas cooling and its chemistry, feedback processes, and the fragmentation of cold gas that triggers the star formation. Interactions between or mergers of galaxies later on influence their ongoing evolution. Whereas the main physical mechanisms seem to be identified by observations, the specific details concerning feedback and baryonic physics, the star formation in particular, are unclear to some extent. Semi-analytic models (SAMs) of galaxies are one way to describe the complex galaxy physics by combining ana-

lytic prescriptions, where possible, with results from numerical simulations of the cosmological dark-matter density field (e.g. Springel et al. 2005 and Henriques et al. 2015, H15 hereafter). With regard to the specific details, SAMs are phenomenological and employ free parameters that have to be calibrated by matching the models to observables, such as the stellar-mass function of galaxies or, as for H15, the fraction of quiescent galaxies as function of redshift.

According to this standard paradigm of galaxy physics, there has to be a strong correlation between the distribution of dark matter and galaxies. The correlation with galaxy type, cosmic time (redshift), spatial scale, and environment is usable statistical information on galaxy physics. An important tool for gathering this information is the weak-gravitational lensing effect that shears the shapes of distant galaxies, so-called sources, through differential light deflection in the tidal gravitational field between the source and the observer (for a review, Schneider et al. 2006). The shear distortion, as described by the theory of general relativity, does not depend on the nature of the gravitating matter. Thus lensing is an ideal probe for dark-matter physics. Although the weak-lensing distortion of single sources is small, recent and ongoing lensing surveys have gathered a sufficient amount of sources to measure the correlations between galaxy and matter

density to a significant level (Aihara et al. 2017; Hildebrandt et al. 2016; Becker et al. 2016; Kuijken et al. 2015; Heymans et al. 2012; Wittman et al. 2006). In addition, a community-wide effort over the last years has produced techniques to accurately measure the lensing distortion in wide-field galaxy surveys (Mandelbaum et al. 2014; Kitching et al. 2012; Bridle et al. 2010; Massey et al. 2007; Heymans et al. 2006).

Galaxy-galaxy lensing (GGL) is one application in weak lensing that considers the correlation between positions of galaxies (lenses) and the shear signal of source galaxies in the background. This is a probe of the radial profile of the surface mass-density of matter around an average lens (e.g. Clampitt et al. 2017; Viola et al. 2015; Choi et al. 2012; Mandelbaum et al. 2006c). As such it can also be used to constrain the population statistics of galaxies inside matter halos, the stellar-mass to halo-mass ratio or, in a modification, the shape of matter halos around single galaxies or group of galaxies (e.g. van Uitert et al. 2017; Schrabback et al. 2015; Coupon et al. 2015; Velander et al. 2014; Gillis et al. 2013; Mandelbaum et al. 2006a,b). Another application employs GGL to quantify the correlation between matter and the galaxy number density on large scales by a second-order biasing function that varies with spatial scale or redshift (e.g. Buddendiek et al. 2016; Prat et al. 2016; Simon 2012; Pen et al. 2003; Hoekstra et al. 2002).

Galaxy-galaxy-galaxy lensing (G3L) is a recent extension of GGL that probes the third-order correlations between the projected matter density and the galaxy number-density with two correlation functions (Simon et al. 2013, 2008; Watts & Schneider 2005; Schneider & Watts 2005). For the scope of this study, we only work with the lens-lens-shear correlation function and use this correlator synonymous with G3L. This kind of G3L is similar to GGL in the sense that it measures the mean tangential shear around pairs of lenses or, after application of a lensing mass-reconstruction, the lensing convergence that is correlated with lens pairs (Simon et al. 2012). Because the lensing convergence is essentially the projected matter density on the sky, the map produced from a G3L signal visualises the typical matter environment of galaxy pairs in projection. With G3L being a connected three-point correlation function by definition, the map shows the convergence in excess of the convergence around two individual galaxies. We therefore refer to this map as ‘excess mass map’ (EMM). Since the introduction of G3L, alternative lensing measures of mass around average lens pairs have also been proposed and obtained from data, partly to probe the filamentary structure of the cosmic web (Epps & Hudson 2017; Clampitt et al. 2016; Johnston 2006).

As discussed in Saghiha et al. (2012) and recently shown by Saghiha et al. (2017), S+17 henceforth, G3L can test SAMs by comparing model predictions for the average matter density around galaxy pairs to measurements. Doing this for galaxies in the CFHTLenS¹ with stellar masses between $\sim 10^9 - 10^{11} M_{\odot}$ and redshifts below $z \lesssim 0.6$, S+17 find the model H15 to be in good agreement while other models strongly disagree with the data. In addition, S+17 argue that for the same data, G3L has more discriminating power in this test than GGL. In particular, the strong dependence on galaxy morphology and galaxy colour makes G3L a powerful test for galaxy models. For testing SAMs, S+17 employ third-order moments of aperture statistics which are an integral transform of the angular G3L correlation function. The aperture statistics quantifies the covariance of fluctuations in the galaxy number density and lensing convergence within apertures of a given angular size. Thereby they are basically the

angular bispectrum of galaxy-galaxy-matter density correlations on the sky (see, for instance, Simon et al. 2013, S+13 hereafter).

We revisit the CFHTLenS data and the most promising synthetic data H15 in S+17 for this paper to gain more insight into the matter-galaxy relation on spatial scales of a few $100 h^{-1}$ kpc. In contrast to S+17, we produce maps of the excess mass. These offer a better intuitive interpretation of the G3L signal by directly mapping out the average surface-matter density that is correlated with lens pairs for a fixed separation of the pair, while the aperture statistics are useful for quantitative measurements of G3L because they are a compressed average of the noisy G3L correlation function for a broad range of separations. We perform measurements of the EMM around CFHTLenS galaxy pairs, optimised with respect to its S/N, and compare these to predictions from the H15 model. Moreover, we introduce a new variant for the excess mass, which we call the ‘pair convergence’ or the pair-convergence map (PCM); it is less affected by unphysical lens pairs that are merely close on the sky in projection (referred to as ‘chance pairs’ in the following).

The structure of the paper is as follows. In Sect. 2, we introduce our notation as well as the definitions of all correlation functions relevant for GGL and G3L. Section 3 introduces the EMM and establishes its relation to the G3L correlation function. Importantly, we discuss the effect of chance pairs on the EMM, and we introduce with the PCM a slightly different definition of the excess mass that is less affected by chance pairs. The two data sets, the simulated mocks and CFHTLenS data, are briefly described in Sect. 4; references to more details are given. In Sect. 5, we then outline in detail two estimators for the EMM (or the PCM) that we apply to CFHTLenS data and simulated H15 data in Sect. 6. By using the two different estimators on simulated data, we verify our computer implementation of the CFHTLenS mapping code. Finally, in Sect. 7, we discuss our conclusions for the excess mass around CFHTLenS pairs and how they qualitatively compare to the H15 predictions.

2. Formalism

2.1. Lensing notation

Let $\delta_m(\mathbf{x})$ be a fluctuation $\delta\rho_m/\bar{\rho}_m$ in the matter-density field $\rho_m(\mathbf{x})$ relative to the mean density $\bar{\rho}_m$ at a comoving position \mathbf{x} . We define positions \mathbf{x} with respect to a fiducial light ray with the observer at the origin (Bartelmann & Schneider 2001). For this, let $\mathbf{x}_{\perp} = f_K(\chi)\boldsymbol{\theta}$ at comoving distance χ be the transverse, comoving separation vector of a neighbour light ray from the fiducial ray, where $f_K(\chi)$ denotes the comoving angular diameter distance and $\boldsymbol{\theta}$ the angular separation of the light ray on the sky. We assume a flat sky and denote angular positions by Cartesian vectors $\boldsymbol{\theta} = \theta_1 + i\theta_2$ in a complex notation with origin $\boldsymbol{\theta} = 0$ in the direction of the fiducial ray. For sources distributed along radial distance χ according to the probability density function (PDF) $p_s(\chi)$, the effective convergence at $\boldsymbol{\theta}$ is a projection of $\delta_m(\mathbf{x})$ onto the sky:

$$\kappa(\boldsymbol{\theta}) = \int_0^{\chi_h} d\chi g(\chi) \delta_m(f_K(\chi)\boldsymbol{\theta}, \chi); \quad (1)$$

$$g(\chi) = \frac{3H_0^2 \Omega_m}{2c^2} \frac{f_K(\chi)}{a(\chi)} \int_{\chi}^{\chi_h} d\chi' p_s(\chi') \frac{f_K(\chi' - \chi)}{f_K(\chi')}, \quad (2)$$

where c is the vacuum speed of light, and H_0 is the Hubble constant; $a(\chi)$ is the scale factor with $a(\chi) = 1$ for $\chi = 0$; and χ_h is the radius of the observable Universe (Schneider et al. 2006).

¹ <http://cfhtlens.org/>

The convergence is related to the (Cartesian) shear field $\gamma_c(\boldsymbol{\theta})$ up to a constant κ_0 through the convolution integral

$$\kappa(\boldsymbol{\theta}) - \kappa_0 = \frac{1}{\pi} \int d^2\theta' \mathcal{D}^*(\boldsymbol{\theta} - \boldsymbol{\theta}') \gamma_c(\boldsymbol{\theta}') =: \kappa_E(\boldsymbol{\theta}) + i\kappa_B(\boldsymbol{\theta}), \quad (3)$$

with the kernel

$$\mathcal{D}^*(\boldsymbol{\theta}) = \frac{\theta_2^2 - \theta_1^2 + 2i\theta_1\theta_2}{|\boldsymbol{\theta}|^4} \quad (4)$$

(Kaiser & Squires 1993). We call the real part $\kappa_E(\boldsymbol{\theta})$ of the convergence the E-mode of the convergence field and the imaginary part $\kappa_B(\boldsymbol{\theta})$ its B-mode. In the weak-lensing regime, lens-lens couplings are negligible so that B-modes serve as indicator of systematic errors for our lensing analysis (Hilbert et al. 2009). In practical studies, we exploit that measurements of the image ellipticity of source galaxies can be made unbiased estimators of γ_c at the positions $\boldsymbol{\theta}$ of the sources if $|\kappa| \ll 1$ (e.g. Simon & Schneider 2017). In the following, we therefore denote by ϵ_i an unbiased estimator of $\gamma_c(\boldsymbol{\theta}_i)$ at the position $\boldsymbol{\theta}_i$ of a source galaxy.

For our analysis, we consider the tangential- and cross-shear components γ_t and γ_\times of $\gamma_c(\boldsymbol{\theta})$ relative to an orientation angle φ , namely we define the φ -rotated shear,

$$\gamma(\boldsymbol{\theta}; \varphi) = -e^{-2i\varphi} \gamma_c(\boldsymbol{\theta}), \quad (5)$$

and its decomposition

$$\gamma_t(\boldsymbol{\theta}; \varphi) + i\gamma_\times(\boldsymbol{\theta}; \varphi) := \gamma(\boldsymbol{\theta}; \varphi). \quad (6)$$

Also, for mathematical convenience, we denote differences between two vectors $\boldsymbol{\theta}_i$ and $\boldsymbol{\theta}_j$ on the flat sky by

$$\boldsymbol{\theta}_{ij} := \boldsymbol{\theta}_i - \boldsymbol{\theta}_j = \theta_{ij} e^{i\varphi_{ij}} \quad (7)$$

with the polar coordinates θ_{ij} and φ_{ij} .

2.2. Galaxy clustering and galaxy-galaxy lensing

In GGL, we correlate positions of lens galaxies with the tangential shear around these galaxies. For this, consider the number density $N_g(\boldsymbol{\theta})$ of lens galaxies on the sky and their density contrast

$$\kappa_g(\boldsymbol{\theta}) = \frac{N_g(\boldsymbol{\theta}) - \bar{N}_g}{\bar{N}_g} \quad (8)$$

relative to the mean number density \bar{N}_g . Similar to $\kappa(\boldsymbol{\theta})$, the density contrast $\kappa_g(\boldsymbol{\theta})$ constitutes a projection along the line-of-sight $\boldsymbol{\theta}$. Concretely, let $\delta_g(\mathbf{x}_\perp, \chi)$ be the relative fluctuations $\delta n_g / \bar{n}_g$ in the three dimensional number density of galaxies at a position relative to the fiducial light ray and $p_d(\chi)$ the PDF of galaxy distances χ inside the observed light cone. Then the density contrast of lenses on the sky is

$$\kappa_g(\boldsymbol{\theta}) = \int_0^{\chi_h} d\chi p_d(\chi) \delta_g(f_K(\chi)\boldsymbol{\theta}, \chi) \quad (9)$$

(e.g., Hoekstra et al. 2002).

Following Peebles (1980), we quantify the second-order angular clustering of lenses by the correlation of two density contrasts at two points with separation ϑ ,

$$\omega(\vartheta) = \langle \kappa_g(\boldsymbol{\theta}) \kappa_g(\boldsymbol{\theta} + \boldsymbol{\vartheta}) \rangle. \quad (10)$$

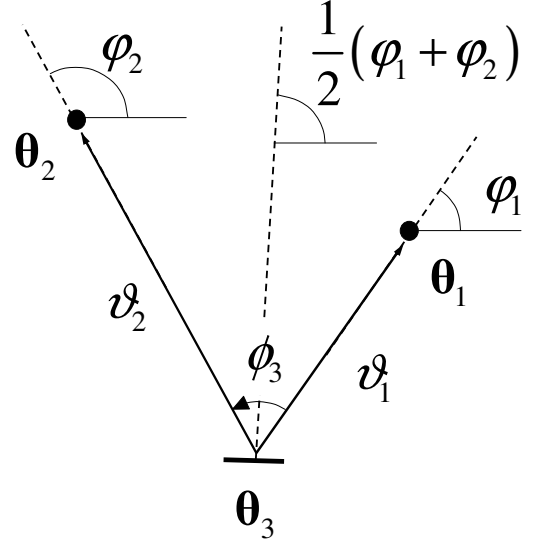


Fig. 1: Geometry in the G3L correlation function \mathcal{G} for lenses at $\boldsymbol{\theta}_1$ and $\boldsymbol{\theta}_2$, and a source at $\boldsymbol{\theta}_3$. The separations between source and lenses are ϑ_1 and ϑ_2 . The separations of the lenses is $\theta_{12} = |\boldsymbol{\theta}_1 - \boldsymbol{\theta}_2|$. This figure is copied from Schneider & Watts (2005).

Owing to statistical isotropy and homogeneity of the random field δ_g , the correlation function $\omega(\vartheta)$ depends only on the separation ϑ of the two points. Likewise, we assume isotropy and homogeneity also for the matter-density fluctuations δ_m so that all following functions that correlate two or more points depend only on the mutual separation of points.

For a cross-correlation of lens positions with the projected matter density, we define the correlation between the number density of lenses and the tangential shear, by which we mean the mean tangential shear

$$\bar{\gamma}_t(\vartheta) = \frac{1}{N_g} \langle N_g(\boldsymbol{\theta}) \gamma(\boldsymbol{\theta} + \boldsymbol{\vartheta}; \varphi) \rangle = \langle \kappa_g(\boldsymbol{\theta}) \gamma(\boldsymbol{\theta} + \boldsymbol{\vartheta}; \varphi) \rangle \quad (11)$$

with φ being the polar angle of $\boldsymbol{\vartheta} = \vartheta e^{i\varphi}$. The imaginary part or cross-component $\bar{\gamma}_\times(\vartheta)$ of this correlator vanishes in the statistical average because of a parity invariance of the random fields (Schneider 2003). Physically, GGL probes the (axis-symmetric) profile of the stacked, that is ensemble-averaged, convergence $\bar{\kappa}(\vartheta) = \langle \kappa_g(\boldsymbol{\theta}) \kappa(\boldsymbol{\theta} + \boldsymbol{\vartheta}) \rangle$ around lenses at separation ϑ , namely

$$\bar{\gamma}_t(\vartheta) = \left(\frac{2}{\vartheta^2} \int_0^\vartheta d\vartheta' \vartheta' \bar{\kappa}(\vartheta') \right) - \bar{\kappa}(\vartheta) \quad (12)$$

(Kaiser 1995).

2.3. Galaxy-galaxy-galaxy lensing

A correlation function similar to GGL can be defined by measuring the average tangential shear at $\boldsymbol{\theta}_3$ around a pair of lenses at $\boldsymbol{\theta}_1$ and $\boldsymbol{\theta}_2$. This is introduced as one of two correlation functions of G3L in Schneider & Watts (2005) by

$$\begin{aligned} \mathcal{G}(\vartheta_1, \vartheta_2, \varphi_3) &= \left\langle \kappa_g(\boldsymbol{\theta}_1) \kappa_g(\boldsymbol{\theta}_2) \gamma \left(\boldsymbol{\theta}_3; \frac{\varphi_1 + \varphi_2}{2} \right) \right\rangle \\ &= -e^{-i(\varphi_1 + \varphi_2)} \left\langle \kappa_g(\boldsymbol{\theta}_1) \kappa_g(\boldsymbol{\theta}_2) \gamma_c(\boldsymbol{\theta}_3) \right\rangle, \end{aligned} \quad (13)$$

where $\phi_3 = \varphi_2 - \varphi_1$ denotes the angle spanned by the two separation vectors $\theta_1 - \theta_3$ and $\theta_2 - \theta_3$ with polar angles φ_1 and φ_2 respectively. Fig. 1 sketches the geometry. The tangential shear is thus defined relative to the line that bisects the angle between the two lenses.

From a mathematical point of view, \mathcal{G} is a correlator between the random field $\kappa_g(\theta)$ at θ_1 and θ_2 , and the random field $\gamma_c(\theta)$ at θ_3 . Since both fields vanish on average, by which we mean that $\langle \kappa_g(\theta) \rangle = \langle \gamma_c(\theta) \rangle = 0$ for all θ , the correlation function \mathcal{G} contains no additive contributions from correlators smaller than third order, the so-called unconnected terms, and thus vanishes for purely Gaussian random fields (e.g. Mo et al. 2010).

3. Mapping of mass correlated with lens pairs

3.1. Definitions of the excess mass

Similar to GGL, the correlator \mathcal{G} can be related to the stacked convergence around lenses, pairs of lenses in this case (Simon et al. 2008, 2013). We show this by considering first the shear pattern around an average lens pair. Stacking the shear field around two lenses at θ_1 and θ_2 results in the average

$$\begin{aligned} \frac{\langle N_g(\theta_1)N_g(\theta_2)\gamma_c(\theta_3) \rangle}{\langle N_g(\theta_1)N_g(\theta_2) \rangle} &= \frac{\langle [1 + \kappa_g(\theta_1)][1 + \kappa_g(\theta_2)]\gamma_c(\theta_3) \rangle}{1 + \omega(\theta_{12})} \\ &= \frac{\langle \kappa_g(\theta_1)\kappa_g(\theta_2)\gamma_c(\theta_3) \rangle + \langle \kappa_g(\theta_1)\gamma_c(\theta_3) \rangle + \langle \kappa_g(\theta_2)\gamma_c(\theta_3) \rangle}{1 + \omega(\theta_{12})}, \end{aligned} \quad (14)$$

where we have used $\langle N_g(\theta)N_g(\theta + \vartheta) \rangle = \bar{N}_g^2(1 + \omega(\vartheta))$; θ_{12} is the separation of the lenses. In order to understand why the left-hand side of (14) equals the average shear around two lens galaxies, one should consider the number-density field of lenses projected on a regular grid with a large number of micro-cells, each with a solid angle σ . Each micro-cell shall be fine enough to contain either no lens or just one lens, which means that $\int_{\sigma} d\sigma N_g(\theta) = 0$ or 1. We then have a contribution to $\langle N_g(\theta_1)N_g(\theta_2)\gamma_c(\theta_3) \rangle$ only for $\int_{\sigma} d\sigma N_g(\theta_1) = \int_{\sigma} d\sigma N_g(\theta_2) = 1$, while $\langle N_g(\theta_1)N_g(\theta_2) \rangle$ in the denominator is the probability to have a pair of galaxies at θ_1 and θ_2 at the same time (normalisation factor).

Now, through the definitions (5) and (11) for GGL we additionally have $\langle \kappa_g(\theta_j)\gamma_c(\theta_3) \rangle = -e^{2i\varphi_j} \bar{\gamma}_t(\vartheta_j)$ and can therefore cast (14) into

$$\begin{aligned} \langle \kappa_g(\theta_1)\kappa_g(\theta_2)\gamma_c(\theta_3) \rangle &= (1 + \omega(\theta_{12})) \frac{\langle N_g(\theta_1)N_g(\theta_2)\gamma_c(\theta_3) \rangle}{\langle N_g(\theta_1)N_g(\theta_2) \rangle} \\ &+ e^{2i\varphi_{13}} \bar{\gamma}_t(\vartheta_1) + e^{2i\varphi_{23}} \bar{\gamma}_t(\vartheta_2). \end{aligned} \quad (15)$$

This shows that \mathcal{G} is, apart from a phase factor, indeed related to the average shear around lens pairs given by the first term on the right-hand side – but rescaled with $1 + \omega(\theta_{12})$ and in excess of the mean shear around individual lenses as given by the two terms that involve $\bar{\gamma}_t$.

For the EMM, we consider a two-dimensional convergence map $\overline{\Delta\kappa_{\text{emm}}}(\vartheta; \theta_{12})$ that corresponds to the excess shear in Eq. (15) around lenses at given separation θ_{12} . We construct this map in a specific coordinate frame, for which ϑ is the relative separation from the map centre O . See the sketch in Fig. 2. The lenses are located at $\theta_1 = -\theta_{12} \mathbf{e}_x/2$ and $\theta_2 = +\theta_{12} \mathbf{e}_x/2$ with \mathbf{e}_x being a unit vector in the x -direction. Applying the linear Kaiser-Squires transformation in Eq. (3) to Eq. (15) in this coordinate

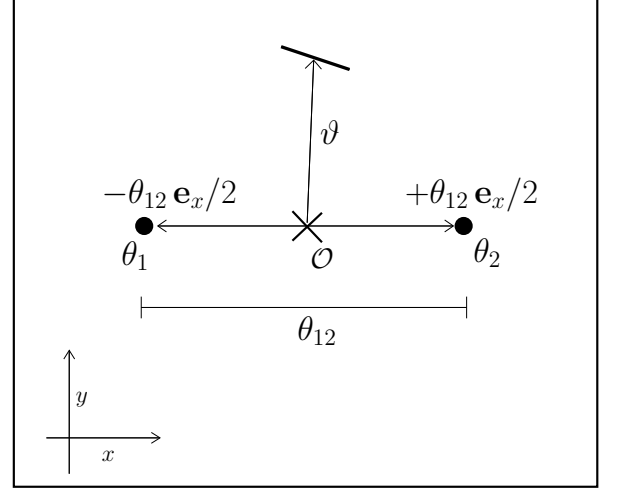


Fig. 2: Cartesian coordinate frame for the EMM or PCM. Lenses with separation θ_{12} are at the positions as indicated by the solid points. A location inside the map is identified by the two-dimensional vector ϑ .

frame, yields, up to a constant κ_0 , a convergence map that can be expanded according to

$$\begin{aligned} \overline{\Delta\kappa_{\text{emm}}}(\vartheta; \theta_{12}) &= (1 + \omega(\theta_{12})) \bar{\kappa}_{\text{pair}}(\vartheta; \theta_{12}) - \bar{\kappa}_{\text{ind}}(|\vartheta - \theta_1|) - \bar{\kappa}_{\text{ind}}(|\vartheta - \theta_2|) + \kappa_0. \end{aligned} \quad (16)$$

Here the average convergence $\bar{\kappa}_{\text{pair}}(\vartheta; \theta_{12})$ around lens pairs corresponds to the shear stack $\langle N_g N_g \gamma_c \rangle / \langle N_g N_g \rangle$ in (15), and the average convergence $\bar{\kappa}_{\text{ind}}(|\vartheta|) = \langle N_g(\theta)\kappa(\theta + \vartheta) \rangle / \bar{N}_g$ around individual lenses corresponds to the average shear $-e^{2i\varphi} \bar{\gamma}_t(|\vartheta|)$, centred on the location of each lens. We emphasise that $1 + \omega(\theta_{12})$ is a constant in this map, and that $\bar{\kappa}_{\text{ind}}(|\vartheta|)$ is by definition of \mathcal{G} the average convergence around *all* galaxies in the sample, including those that do not have a partner at separation θ_{12} .

Since the relation between $\kappa(\theta)$ and $\gamma_c(\theta)$ is degenerate, we cannot uniquely determine the EMM from the excess shear. See Eq. (3). It is, however, reasonable to assume that $\overline{\Delta\kappa_{\text{emm}}}(\vartheta; \theta_{12})$, being the three-point correlation function $\langle \kappa_g \kappa_g \gamma_c \rangle$, quickly approaches zero for large ϑ which might be used to define κ_0 . Alternatively, for the maps presented here, we fix κ_0 by asserting that $\overline{\Delta\kappa_{\text{emm}}}$ vanishes when averaged over the entire map area. We will neglect κ_0 in the following equations for convenience.

For what follows, we also consider as variant of the EMM the ‘pair convergence’, or the PCM of lens pairs, which is the straightforward difference signal

$$\begin{aligned} \overline{\Delta\kappa}(\vartheta; \theta_{12}) &:= \bar{\kappa}_{\text{pair}}(\vartheta; \theta_{12}) - \bar{\kappa}_{\text{ind}}(|\vartheta - \theta_1|) - \bar{\kappa}_{\text{ind}}(|\vartheta - \theta_2|) \\ &= \overline{\Delta\kappa_{\text{emm}}}(\vartheta; \theta_{12}) - \omega(\theta_{12}) \bar{\kappa}_{\text{pair}}(\vartheta; \theta_{12}) \end{aligned} \quad (17)$$

between the stacked convergence around lens pairs and the stacked convergence around two individual lenses. Since the EMM, originating from the connected correlation function \mathcal{G} , is free of unconnected correlations by definition, our interpretation is that the EMM is the connected part of the PCM, and the extra term $-\omega(\theta_{12}) \bar{\kappa}_{\text{pair}}(\vartheta; \theta_{12})$ is the unconnected part of the PCM.

While the EMM exactly vanishes for Gaussian random fields, the PCM generally does not although it is entirely determined by second-order correlations in this case. This can be seen from the definition (17) of $\overline{\Delta\kappa}$ and Eq. (16) with $\overline{\Delta\kappa_{\text{emm}}} = 0$, giving

$$\overline{\Delta\kappa}(\boldsymbol{\theta}; \theta_{12}) = -\frac{\omega(\theta_{12})}{1 + \omega(\theta_{12})} \left(\overline{\kappa}_{\text{ind}}(|\boldsymbol{\theta} - \boldsymbol{\theta}_1|) + \overline{\kappa}_{\text{ind}}(|\boldsymbol{\theta} - \boldsymbol{\theta}_2|) \right). \quad (18)$$

We visualise the excess mass as a two-dimensional map by plotting either $\overline{\Delta\kappa_{\text{emm}}}$, for the EMM, or $\overline{\Delta\kappa}$, for the PCM, as function of $\boldsymbol{\theta}$ for a fixed lens-lens separation θ_{12} and orientation. The resulting maps have two known symmetries (Simon et al. 2008). First, there is a parity symmetry: correlation functions are unchanged under a reflection of shear and the lens density across an axis owing to the parity invariance of cosmological fields (Schneider 2003). As a consequence, quadrants in the maps are statistically consistent when mirrored across the line connecting two lenses. Second, another symmetry is present because we correlate density fluctuations κ_g at $\boldsymbol{\theta}_1$ and $\boldsymbol{\theta}_2$ from the same galaxy sample: a permutation of lens indices results in the same correlation function. Both combined produce in the absence of noise an exact reflection symmetry of the map with respect to the x - and y -axis. We exploit this symmetry to enhance the S/N in the maps by averaging the quadrants inside the maps.

Physically the dimensionless quantities $\overline{\Delta\kappa_{\text{emm}}}$ and $\overline{\Delta\kappa}$ are surface-mass densities in units of the (average) critical density $\overline{\Sigma}_{\text{crit}}$, defined by

$$\overline{\Sigma}_{\text{crit}}^{-1} := \frac{4\pi G_{\text{N}}}{c^2} \int_0^{\chi_{\text{h}}} d\chi_s d\chi_d p_d(\chi_d) p_s(\chi_s) \frac{a(\chi_d) f_K(\chi_d) f_K(\chi_s - \chi_d)}{f_K(\chi_s)}, \quad (19)$$

where G_{N} is Newton's gravitational constant. In our analysis, lenses have a typical distance of $z_d \approx 0.4$ and sources of $z_s \approx 0.93$ so that we estimate $\overline{\Sigma}_{\text{crit}} \approx 4.25 \times 10^3 h M_{\odot} \text{pc}^{-2}$ as fiducial value for the following.

3.2. Impact of chance galaxy pairs

The following is a simplified discussion to explore the impact of uncorrelated lens pairs on an EMM or a PCM. In the construction of our maps, we select galaxy pairs from a given sample by their angular separation θ_{12} on the sky. Therefore, there will be pairs that are well separated in radial distance from each other, such that third-order correlations involving these are negligible for practical purposes. On the other hand, we will have pairs, which have non-negligible third-order correlations with the lensing convergence as they are at similar distance. Obviously, we cannot make a clear distinction between these two types of pairs because of the vague term 'negligible' although, in practice, we arguably could define a reasonable threshold for the correlation amplitude or the radial separation of galaxies in a pair. For the purpose of a simplified discussion here, however, we assume that in a sample of lenses we have a fraction $1 - p_{\text{tp}}$ of pairs for which a stack of convergence shall be free of any third-order correlations so that we find the expectation value

$$\overline{\kappa}_{\text{pair}}(\boldsymbol{\theta}; \theta_{12}) = \overline{\kappa}_{\text{ind}}(|\boldsymbol{\theta} - \boldsymbol{\theta}_1|) + \overline{\kappa}_{\text{ind}}(|\boldsymbol{\theta} - \boldsymbol{\theta}_2|) =: \overline{\kappa}_{\text{pair}}(\boldsymbol{\theta}; \theta_{12})|_{\text{cp}}. \quad (20)$$

These are the 'chance pairs' (CP). The remaining fraction p_{tp} of (physically connected) pairs, to which we refer as 'true pairs' (TP), shall have a different yet unspecified stack

$\overline{\kappa}_{\text{pair}}(\boldsymbol{\theta}; \theta_{12}) = \overline{\kappa}_{\text{pair}}(\boldsymbol{\theta}; \theta_{12})|_{\text{tp}}$ that depends in detail on the average surface mass-density around those pairs and the critical density $\overline{\Sigma}_{\text{crit}}$ at the distance of the pair. The stack around TP carries the interesting physical information so that, ideally, we would like to define an excess mass that is independent from CP. This is neither true for EMM nor for PCM.

We look at pure CP or TP samples first. For pure CP samples, that means $p_{\text{tp}} = 0$, the EMM and PCM vanish because mass cannot be correlated with two statistically independent lenses. Indeed, we will find $\overline{\kappa}_{\text{pair}}(\boldsymbol{\theta}; \theta_{12}) = \overline{\kappa}_{\text{pair}}(\boldsymbol{\theta}; \theta_{12})|_{\text{cp}}$, $\omega(\theta_{12}) = 0$, and consequently $\overline{\Delta\kappa_{\text{emm}}} = \overline{\Delta\kappa} = 0$. On the other hand, if we have a pure TP sample ($p_{\text{tp}} = 1$) with a clustering amplitude ω_{tp} (at separation θ_{12}), we will find

$$\begin{aligned} \overline{\Delta\kappa_{\text{emm}}}(\boldsymbol{\theta}; \theta_{12}) &= \\ &= (1 + \omega_{\text{tp}}) \overline{\kappa}_{\text{pair}}(\boldsymbol{\theta}; \theta_{12})|_{\text{tp}} - \overline{\kappa}_{\text{ind}}(|\boldsymbol{\theta} - \boldsymbol{\theta}_1|) - \overline{\kappa}_{\text{ind}}(|\boldsymbol{\theta} - \boldsymbol{\theta}_2|) \\ &=: \overline{\Delta\kappa_{\text{emm}}}(\boldsymbol{\theta}; \theta_{12})|_{\text{tp}} \end{aligned} \quad (21)$$

for the EMM. We obtain the equation for $\overline{\Delta\kappa}(\boldsymbol{\theta}; \theta_{12})$ by setting ω_{tp} to zero in (21).

Usually we have a mixture of CP and TP, and the impact of CP on the EMM is not immediately obvious. To explore this case, let us now assume that $0 < p_{\text{tp}} < 1$ and that the GGL is as in the foregoing pure samples. In this mixture, the clustering amplitude is reduced to $\omega = p_{\text{tp}} \omega_{\text{tp}}$, and the convergence stack around all pairs,

$$\overline{\kappa}_{\text{pair}}(\boldsymbol{\theta}; \theta_{12}) = p_{\text{tp}} \overline{\kappa}_{\text{pair}}(\boldsymbol{\theta}; \theta_{12})|_{\text{tp}} + (1 - p_{\text{tp}}) \overline{\kappa}_{\text{pair}}(\boldsymbol{\theta}; \theta_{12})|_{\text{cp}}, \quad (22)$$

is weighted average of the stacks in the pure samples. Then using (20)-(22) in Eq.(16) results, after some algebra, in the EMM of a mixed sample:

$$\begin{aligned} \overline{\Delta\kappa_{\text{emm}}}(\boldsymbol{\theta}; \theta_{12}) &= \\ &= p_{\text{tp}} \frac{1 + p_{\text{tp}} \omega_{\text{tp}}}{1 + \omega_{\text{tp}}} \overline{\Delta\kappa_{\text{emm}}}(\boldsymbol{\theta}; \theta_{12})|_{\text{tp}} \\ &+ p_{\text{tp}} (1 - p_{\text{tp}}) \frac{\omega_{\text{tp}}^2}{1 + \omega_{\text{tp}}} \left(\overline{\kappa}_{\text{ind}}(|\boldsymbol{\theta} - \boldsymbol{\theta}_1|) + \overline{\kappa}_{\text{ind}}(|\boldsymbol{\theta} - \boldsymbol{\theta}_2|) \right). \end{aligned} \quad (23)$$

In conclusion, while the presence of CP merely diminishes the overall amplitude of the TP excess-mass $\overline{\Delta\kappa_{\text{emm}}}(\boldsymbol{\theta}; \theta_{12})|_{\text{tp}}$ in the mixture, there is also a second term in the last line of Eq. (23) that changes the overall appearance of the map by adding an extra signal, mainly at the lens positions, that is proportional to the convergence stack around CP.

This extra signal can be avoided in the PCM. Namely, by plugging (20) and (22) into Eq. (17) we get

$$\overline{\Delta\kappa}(\boldsymbol{\theta}; \theta_{12}) = p_{\text{tp}} \left(\overline{\kappa}_{\text{pair}}(\boldsymbol{\theta}; \theta_{12})|_{\text{tp}} - \overline{\kappa}_{\text{ind}}(|\boldsymbol{\theta} - \boldsymbol{\theta}_1|) - \overline{\kappa}_{\text{ind}}(|\boldsymbol{\theta} - \boldsymbol{\theta}_2|) \right) \quad (24)$$

for a mixture sample: The presence of CP does at most change the overall amplitude in the PCM; each value in the map gives a lower limit to the pair convergence around TP inside the brackets of (24).

4. Data

4.1. The Canada-France-Hawaii Telescope Lensing Survey

The CFHTLenS is a multi-colour, wide-field lensing survey with measurements of galaxy photometry in the five bands $u^*g'r'i'z'$ (AB system), observed as part of the CFHT Legacy Survey Wide (Heymans et al. 2012). The survey covers 154 deg^2 of the

sky, consisting of four contiguous fields: W1 ($\approx 64 \text{ deg}^2$), W2 ($\approx 23 \text{ deg}^2$), W3 ($\approx 44 \text{ deg}^2$), and W4 ($\approx 23 \text{ deg}^2$). The seeing is optimised for lensing measurements in the r' -band and lies typically between $0.66'' - 0.82''$; the camera resolution is $0.187''$ per CCD pixel. Each field is a mosaic of a set of Megacam pointings with $1 \times 1 \text{ deg}^2$ field-of-view each. The data reduction uses the processing pipeline THELI (Erben et al. 2013); shear measurements of source galaxies are done employing *lensfit* (Miller et al. 2013); estimates for galaxies redshifts and stellar masses are obtained by the method of photometric redshifts for a PSF-matched photometry and by using the computer code BPZ (Hilbrandt et al. 2012, Benitez 2000). The final galaxy catalogue comprises physical parameters of 7×10^6 objects, including estimates of stellar masses, photometric redshifts, and shear estimates.² For our analysis, we use only Megacam pointings that are flagged as ‘good’ for lensing studies. This amounts to roughly 75 per cent of the pointings with an effective area of $A \approx 95 \text{ deg}^2$, which we determined by counting the number of unmasked pixels in the mask files of the 129 good pointings. For the selection of lens and source catalogues, we follow the criteria in S+13 where several tests for systematic errors in the G3L measurements for our samples are already performed. See also S+13 for plots of the redshift distributions of galaxy samples.

Our source samples are galaxies with $i' < 24.7$, photometric redshifts between $0.65 \leq z_{\text{ph}} < 1.2$, and non-vanishing statistical weights w_i according to *lensfit*. This gives roughly 2.2×10^6 sources inside the good pointings and a mean, w -weighted redshift of $\bar{z}_s \approx 0.93$. The lower limit in z_{ph} is chosen to reduce the overlap in redshift between lens and source samples in order to suppress systematic errors in the correlation functions. The effective number density of our sources is $\bar{N}_s = (\sum_i w_i)^2 / (A \sum_i w_i^2) \approx 5.5 \text{ arcmin}^{-2}$. To correct for the additive and multiplicative bias m_i in the estimators ϵ_i of the shear of the i th source, we follow the instructions in Miller et al. (2013). For this, the correction for m_i is easily included in our shear-related estimators by replacing $\epsilon_i \mapsto \epsilon_i (1 + m_i)^{-1}$ and $w_i \mapsto w_i (1 + m_i)$; we always have $m_i > -1$ (Appendix A in S+13).

For the lens samples, we select galaxies with flux limit $i' < 22.5$ from two photo- z bins: $0.2 \leq z_{\text{ph}} < 0.44$ (‘low- z ’) and $0.44 \leq z_{\text{ph}} < 0.6$ (‘high- z ’). In addition, we select galaxies only from the stellar-mass range between $5 \times 10^9 - 3.2 \times 10^{11} M_\odot$ which combines all stellar-mass samples sm1 to sm6 in S+13. The estimates for stellar masses assume an initial-mass function according to Chabrier (2003) and have a typical RMS error of 0.3 dex (Velander et al. 2014). Counting only good pointings, we have in total 1.8×10^5 galaxies in the low- z sample, yielding $\bar{N}_g \approx 0.5 \text{ arcmin}^{-2}$, and 2.5×10^5 galaxies in the high- z sample, $\bar{N}_g \approx 0.7 \text{ arcmin}^{-2}$. The mean redshifts are $\bar{z}_d \approx 0.35, 0.51$ for low- z and high- z . The RMS error of the redshift estimates is given by $\sigma(z) \approx 0.04 (1 + z)$ with an outlier rate of roughly 3%.

The lower limit of allowed stellar masses in addition to the $i' < 22.5$ flux limit makes our lens sample approximately volume-limited inside the redshift intervals, as can be seen from the plots in the Fig. A.1 in the Appendix. The figure depicts scatter plots of absolute rest-frame magnitudes and colours versus redshift for the CFHTLenS galaxies; the blue dots are galaxies with stellar-mass selection, the orange dots galaxies without stellar-mass selection. Only the few galaxies that are fainter than $M_u \gtrsim -18.5$ or $M_g \gtrsim -19.5$ are missing for $z_B \gtrsim 0.4$, i.e., for high- z , while most stellar-mass limited objects are brighter than the flux-limit, which is indicated by the locus of orange

points at faint magnitudes. By comparing the distribution of blue and orange points in the colour plots we also see that the stellar-mass selection rejects galaxies bluer than $M_g - M_r \lesssim 0.3$ or $M_u - M_g \lesssim 0.6$ at all redshifts (left column in figure).

4.2. Synthetic lensing data and mock galaxies

Our mock lensing-data are generated by tracing the distortion of light bundles that traverse 64 independent light cones of the N -body Millennium Simulation (Springel et al. 2005, MS hereafter; Hilbert et al. 2009). The MS is a purely dark-matter simulation with a spatial (comoving) resolution of $5 h^{-1} \text{ kpc}$ that is sampled by $\sim 10^{10}$ mass particles, populating a cubic region of comoving side length of $500 h^{-1} \text{ Mpc}$. The fiducial cosmology of the MS has the following parameters: $\Omega_m = 0.25 = 1 - \Omega_\Lambda$ for density parameters of matter and dark energy; $\Omega_b = 0.045$ for the baryon density; $\sigma_8 = 0.9$ for the normalisation of the linear matter power spectrum at $z = 0$; a Hubble parameter of $H_0 = h 100 \text{ km s}^{-1} \text{ Mpc}^{-1}$ with $h = 0.73$; and primordial fluctuations as in the Harrison-Zeldovich model. The fiducial cosmology in the MS is somewhat different compared to recent results by the Planck Collaboration et al. (2016), which for our qualitative comparison of the excess mass around galaxy pairs, however, is not of great relevance.

Regarding the synthetic lensing data, the simulated light-bundle distortions are an average for source distances with a probability distribution as that for the CFHTLenS sources (see Fig. 5 in S+13). Each of the 64 simulated light cones yields a regular, quadratic grid with information on the theoretical lensing convergence and shear along the line-of-sight of 4096^2 pixel positions; a grid covers a solid angle of $4 \times 4 \text{ deg}^2$ on the sky. The total area of the mock data is therefore 1024 deg^2 . We mainly use the convergence grid for the estimator in Sect. 5.3. Only in one case, where we compare the convergence-stack method to the shear-stack method, Sect. 5.1, we also generate synthetic shear catalogues. For these, we uniformly pick random positions of sources on the grid and assign the shear value closest to the position as source ellipticity. This means we do not include shape noise.

For mock lens-galaxies, we apply the H15 SAM-description to the MS that is adjusted to the fiducial cosmology of the MS. We then follow the steps in S+17, Sect. 3.2 therein, to obtain the mock lens-samples low- z and high- z with a selection function that is consistent with that of galaxies in CFHTLenS, including an emulation of statistical errors in both stellar masses and photometric redshifts. In particular, the mock samples have redshift distributions that are consistent with the CFHTLenS samples.

5. Estimators of excess mass

We present two versions of estimators for the EMM, Eq. (16), and the PCM, Eq. (17), which aim for different applications. In one version, we stack the shear field around pairs of galaxies and carry out a convergence reconstruction of the stack afterwards. This approach is suitable for observational weak-lensing data where only estimates of (reduced) shear are available for a set of discrete positions of source galaxies. In another version, we stack the convergence on contiguous grids directly, either for quick model predictions of the excess mass or to assess the accuracy of the shear-stacking method.

For practical implementations of both estimators, we note that frequently occurring phase factors $e^{2i\varphi_{ij}}$ of separation vectors

² <http://www.cadc-ccda.hia-ihp.nrc-cnrc.gc.ca/en/community/CFHTLenS/query.html>

in our usual complex notation $\theta_{ij} = \theta_{ij} e^{i\varphi_{ij}}$ are easily computed by $e^{2i\varphi_{ij}} = \theta_{ij}/\theta_{ij}^*$.

5.1. Shear stack

Let θ_i^d be positions of n_d lens galaxies on the sky, and $(\epsilon_i, w_i, \theta_i^s)$ the details of n_s source galaxies with ellipticities ϵ_i , statistical weights w_i , and positions θ_i^s . From this, we compute the excess shear in Eq. (15) that is based on both the shear stack around galaxy pairs – the first term of the right-hand side of this equation – and the average shear around individual galaxies, which are the other terms on the right-hand side. Importantly, the excess shear is not identical to the average shear around galaxy pairs; it is usually only a small fraction of the latter.

The overall strategy for an estimator of the EMM is: (i) we estimate the excess shear by stacking source ellipticities around lens pairs in an appropriate reference frame and with weights $1 + \omega(\theta_{12})$ (first term in Eq. 15) and (ii) add the terms that involve $\bar{\gamma}_t(\vartheta)$ to the stack (other terms); (iii) we apply the Kaiser-Squires inversion, Eq. (3), to obtain the EMM in Eq. (16); (iv) finally, we subtract a constant κ_0 from the map. The computation of the pair convergence is only slightly different as we explicitly set $\omega(\theta_{12}) \equiv 0$ in this procedure. The following describes the details of the stacking and the convergence reconstruction. Therein we assume that estimates of $\omega(\vartheta)$ and $\bar{\gamma}_t(\vartheta)$ are already available; see the following section for estimators of those.

For stacking, we define a two-dimensional grid with $N_p \times N_p$ grid pixels (we choose $N_p = 200$); pixels shall have a square geometry. Each grid cell mn has the vector position $\mathbf{p}_{mn} = m + i n$ where (m, n) are its coordinates in a Cartesian stacking frame. Let (θ_i^d, θ_j^d) be the positions of a selected lens pair ij within the separation bin $\vartheta - \Delta\vartheta/2 \leq |\theta_i^d - \theta_j^d| < \vartheta + \Delta\vartheta/2$, and $(\epsilon_k, w_k, \theta_k^s)$ are the details of a source close to the lens pair. We map θ -coordinates to \mathbf{p} -coordinates by a rotation α_{ij} and scaling $|A_{ij}|$, both encapsulated inside $A_{ij} = |A_{ij}| e^{i\alpha_{ij}}$, and a translation B_{ij} ,

$$\mathbf{p} = A_{ij} \theta + B_{ij}. \quad (25)$$

The complex-valued parameters A_{ij} and B_{ij} are determined by the mapping of the two lens positions to the fixed positions \mathbf{p}_1^d and \mathbf{p}_2^d in the stack,

$$A_{ij} = \frac{\mathbf{p}_2^d - \mathbf{p}_1^d}{\theta_j^d - \theta_i^d}; \quad B_{ij} = \frac{\theta_j^d \mathbf{p}_1^d - \theta_i^d \mathbf{p}_2^d}{\theta_j^d - \theta_i^d} \quad (26)$$

(see Fig. 3 for an illustration). The positions of sources θ_k^s are therefore $\mathbf{p}_{ijk}^s = A_{ij} \theta_k^s + B_{ij}$ in the stacking frame. Additionally, the source ellipticities ϵ_k have to be rotated by $\epsilon_k \mapsto e^{2i\alpha_{ij}} \times \epsilon_k = A_{ij}/A_{ij}^* \times \epsilon_k$ in the \mathbf{p} -frame. Before mapping ϵ_k to the stacking frame we subtract off the average shear around each lens position in the θ -frame to obtain the excess shear. The complete stack for the excess shear at the grid pixel mn is then the weighted sum

$$\Delta\gamma_{mn} = \sum_{i,j,k=1}^{n_d, n_s} \frac{\Delta_{ijk}^{mn} w_k e^{2i\alpha_{ij}}}{W_{mn}} \left([1 + \omega(\theta_{ij}^{dd})] \epsilon_k + e^{2i\varphi_{ik}} \bar{\gamma}_t(\theta_{ik}^{ds}) + e^{2i\varphi_{jk}} \bar{\gamma}_t(\theta_{jk}^{ds}) \right), \quad (27)$$

where the total weight is

$$W_{mn} = \sum_{i,j,k=1}^{n_d, n_s} \Delta_{ijk}^{mn} w_k, \quad (28)$$

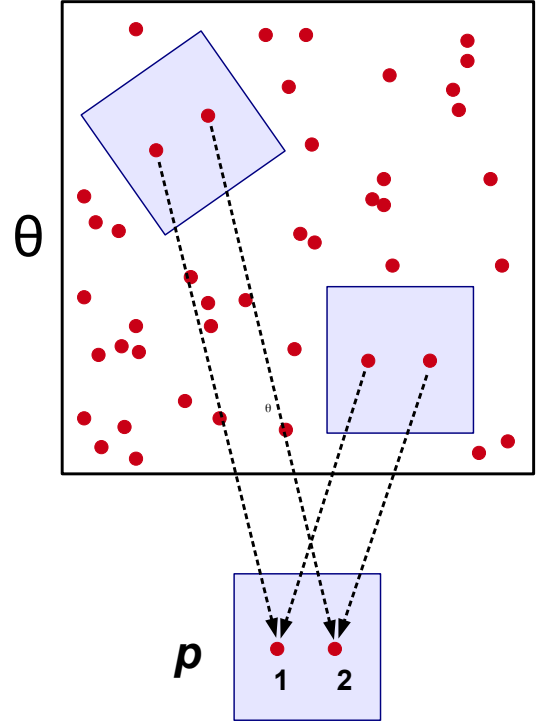


Fig. 3: Schematic of the stacking procedure. Positions θ on the sky are mapped to stacking frame positions \mathbf{p} defined by the fixed positions of a selected lens pair (red points) in the stacking frame. The stacking-frame positions of the lenses are denoted by \mathbf{p}_1^d and \mathbf{p}_2^d . The mapping involves a rotation so that source ellipticities in the stack have to be rotated.

and $\Delta_{ijk}^{mn} = 1$ flags if the source position \mathbf{p}_{ijk}^s falls within the grid cell mn and $\Delta_{ijk}^{mn} = 0$ otherwise; by θ_{ij}^{dd} we denote the separation between the lenses i and j , and by θ_{ik}^{ds} the difference vector between the lens i and the source k ; the angle φ_{ik} is the polar angle of $\theta_{ik}^{ds} = \theta_{ik}^{ds} e^{i\varphi_{ik}}$.

We then convert the stack $\Delta\gamma_{mn}$ of excess shear into a map of the excess convergence. Owing to a sparse sampling of the shear stack by discrete source positions around lens pairs, an additional smoothing of this map is required. We apply this smoothing with a kernel K to $\Delta\gamma_{mn}$ before the conversion to the EMM or PCM, namely by means of

$$\Delta\gamma_{mn}^K = \frac{\sum_{n', m'=1}^{N_p, N_p} W_{m'n'} K(m - m', n - n') \Delta\gamma_{m'n'}}{\sum_{n', m'=1}^{N_p, N_p} W_{m'n'} K(m - m', n - n')} \quad (29)$$

for the Gaussian kernel

$$K(\delta m, \delta n) = \exp\left(-\frac{1}{2} \frac{\delta m^2 + \delta n^2}{\sigma_{\text{rms}}^2}\right) \quad (30)$$

which has the kernel size σ_{rms} in units of our grid-pixel size. Using the weights W_{mn} for the smoothing ignores grid pixel with no shear information and gives more weight to pixels with a higher

W_{mn} in the average of neighbouring pixels. We use a smoothing scale of $\sigma_{\text{rms}} = 4$ for our maps.

In the last step, we apply the algorithm by Kaiser & Squires (1993) to $\Delta\gamma_{mn}^K$ on the grid, employing Fast-Fourier Transformations, to obtain the a smoothed map $\widehat{\Delta\kappa_{mn}^K} = \Delta\kappa_{mn}^K + \kappa_0$ of the excess convergence with a constant offset κ_0 . The real part in the excess convergence contains the E-mode of the signal, and the imaginary part is the B-mode. Applying the Kaiser-Squires technique on a finite field produces systematic errors which typically have the effect of increasing the signal towards the edges. We therefore remove 50 pixel from the outer edges of the grid in the final map. The inner cropped map has then the dimensions $100 \times 100 \text{ pixel}^2$. The constant offset κ_0 depends on the details of the implementation of the Kaiser-Squire algorithm and the number N_p of grid pixels. To have consistent maps in the following, we assert that the average excess-convergence over the cropped map has to vanish. We therefore subtract this average from the final map.

5.2. GGL and lens clustering

The second-order statistics $\bar{\gamma}_t(\vartheta)$ and $\omega(\vartheta)$ are estimated from the data by the following standard techniques. For the angular correlation function $\omega(\vartheta)$ of the lens galaxies, we prepare a mock catalogue with n_r uniform random positions within the unmasked region of the survey. We then count the number $DD(\vartheta; \Delta\vartheta)$ of lens pairs within the separation bin $[\vartheta - \Delta\vartheta/2, \vartheta + \Delta\vartheta/2)$, the number of random-galaxy pairs $RD(\vartheta; \Delta\vartheta)$, and the number of random-random pairs $RR(\vartheta; \Delta\vartheta)$. For the count rates, we consider all permutations of galaxy and mock positions, which means the total number of DD , RR , and DR for all separations equals $n_d(n_d - 1)$, $n_r(n_r - 1)$, and $n_d n_r$, respectively. According to Landy & Szalay (1993), we then estimate (for $n_d, n_r \gg 1$)

$$\omega(\vartheta; \Delta\vartheta) = \frac{n_r^2}{n_d^2} \frac{DD(\vartheta; \Delta\vartheta)}{RR(\vartheta; \Delta\vartheta)} - 2 \frac{n_r}{n_d} \frac{DR(\vartheta; \Delta\vartheta)}{RR(\vartheta; \Delta\vartheta)} + 1 \quad (31)$$

for the angular clustering of lenses at separation ϑ .

To measure the mean tangential shear $\bar{\gamma}_t$ and the cross shear $\bar{\gamma}_\times$ within the separation bin $[\vartheta - \Delta\vartheta/2, \vartheta + \Delta\vartheta/2)$, we apply the estimator

$$\bar{\gamma}_t(\vartheta; \Delta\vartheta) + i \bar{\gamma}_\times(\vartheta; \Delta\vartheta) = \frac{\sum_{d,s=1}^{n_d, n_s} \Delta_{ds}(\vartheta; \Delta\vartheta) w_s (-e^{-2i\varphi_{ds}} \epsilon_s)}{\sum_{d,s=1}^{n_d, n_s} \Delta_{ds}(\vartheta; \Delta\vartheta) w_s}, \quad (32)$$

where $e^{-2i\varphi_{ds}} = \theta_{ds}^*/\theta_{ds}$ is the phase factor of $\theta_{ds} = \theta_s^s - \theta_d^d$ and $\Delta_{ds}(\vartheta; \Delta\vartheta) = 1$ for $\vartheta - \Delta\vartheta/2 \leq \theta_{ds} < \vartheta + \Delta\vartheta/2$ and $\Delta_{ds}(\vartheta; \Delta\vartheta) = 0$ otherwise (e.g. Bartelmann & Schneider 2001).

5.3. Convergence stack

In a variant of the previous estimator for maps of the excess mass, we stack the excess convergence $\Delta\bar{\kappa}_{\text{emmm}}$ or $\Delta\bar{\kappa}$ around lens pairs in simulated data directly. Let θ_i^d be the positions of n_d lens galaxies and $\kappa(\theta)$ a simulated grid of convergence values. Similar to Sect. 5.1, we use a shear-free affine transformation to map θ positions around a given pair ij of lenses to the stacking frame with coordinates \mathbf{p} . The estimation process proceeds in four steps: (i) we stack the convergence around a set of selected lens pairs from the separation bin $\vartheta - \Delta\vartheta/2 \leq |\theta_i^d - \theta_j^d| < \vartheta + \Delta\vartheta/2$ to obtain $\bar{\kappa}_{\text{pair}}$; (ii) we stack the convergence around individual lenses to obtain $\bar{\kappa}_{\text{ind},1} + \bar{\kappa}_{\text{ind},2}$ in the stacking frame; (iii)

we estimate $1 + \omega$ averaged for the distribution of lens-lens separations in the sample of selected lens pairs; and (iv) we combine the steps (i) to (iii) to compute the EMM $\Delta\bar{\kappa}_{\text{emmm}} = (1 + \omega)\bar{\kappa}_{\text{pair}} - \bar{\kappa}_{\text{ind},1} - \bar{\kappa}_{\text{ind},2}$ with an estimate of ω , which is averaged over the distribution of lens-lens separations in the stack. As before, setting $\omega \equiv 0$ in (iii) yields the PCM.

For the steps (i) and (ii), we use square grids with $N_p \times N_p$ pixels and coordinates $\mathbf{p}_{mn} = m + in$. The lens positions are defined to be at the fixed location \mathbf{p}_1^d and \mathbf{p}_2^d . Using the definitions (26) for the parameters of the mapping between the \mathbf{p} -frame and the θ -frame for a given lens pair ij , we obtain

$$\theta_{ij}^{mn} = A_{ij}^{-1}(\mathbf{p}_{mn} - B_{ij}) \quad (33)$$

for the position θ in the convergence grid that corresponds to the stack position \mathbf{p}_{mn} . We then compute the stack $\bar{\kappa}_{\text{pair}}$ for the grid pixel mn by the average

$$\bar{\kappa}_{\text{pair}}^{mn} = \frac{\sum_{i,j=1}^{n_d} \Delta_{ij}^{mn} \kappa(\theta_{ij}^{mn})}{\sum_{i,j=1}^{n_d} \Delta_{ij}^{mn}}, \quad (34)$$

where $\Delta_{ij}^{mn} = 1$ indicates if θ_{ij}^{mn} is inside the κ -grid or $\Delta_{ij}^{mn} = 0$ otherwise. In case of $\Delta_{ij}^{mn} = 1$, we choose the grid point in $\kappa(\theta)$ that is closest to θ_{ij}^{mn} .

To obtain a map of the average convergence around individual lenses in step (ii), we have to factor in that the convergence around pairs in the stack is differently scaled for any new lens pair in the stack. Therefore, to obtain $\bar{\kappa}_{\text{ind},1} + \bar{\kappa}_{\text{ind},2}$ for a distribution of scale parameters $|A_{ij}|$ we apply the following technique. For each lens galaxy at θ_i^d , we randomly pick a position $\theta_i^{\text{nd}} = \theta_i^d + \delta\theta_i e^{i\phi_i}$ for an ‘imaginary’ uncorrelated lens, where ϕ_i defines a uniformly random orientation $\phi_i \in [0, 2\pi)$ and $\delta\theta_i$ is a random separation from the i th lens. For $\delta\theta_i$, we randomly pick a separation $|\theta_k^d - \theta_l^d|$ from a list of all separations of selected lens pairs in the data. This assures that (ii) consistently uses the same distribution of rescalings $|A_{ij}|$ that are applied in step (i). Since the positions of imaginary lenses are uncorrelated with both $\kappa(\theta)$ and the lens positions, a stack around lens-imaginary pairs yields (on average) $\bar{\kappa}_{\text{ind},1}$ if the lens is mapped to \mathbf{p}_1^d and the imaginary lens mapped to \mathbf{p}_2^d ; we obtain $\bar{\kappa}_{\text{ind},2}$ if we swap the lens positions in the stack. Therefore, by adding the maps for both cases we obtain the stack $\bar{\kappa}_{\text{ind}} = \bar{\kappa}_{\text{ind},1} + \bar{\kappa}_{\text{ind},2}$, which justifies the estimator

$$\bar{\kappa}_{\text{ind}}^{mn} = \frac{\sum_{i=1}^{n_d} \Delta_{ij}^{mn} \kappa(\theta_{ij}^{mn})}{\sum_{i=1}^{n_d} \Delta_{ij}^{mn}} + \frac{\sum_{i=1}^{n_d} \Delta_{ji}^{mn} \kappa(\theta_{ji}^{mn})}{\sum_{i=1}^{n_d} \Delta_{ji}^{mn}}, \quad (35)$$

where Δ_{ij}^{mn} and θ_{ij}^{mn} are defined as before with the exception that we use $\theta_j^d \equiv \theta_i^{\text{nd}}$ for the position of the second lens in the lens pair ij .

Finally, we combine the information from the previous steps to compute the EMM around the lens pairs by

$$\Delta\bar{\kappa}_{\text{emmm}}^{mn} = [1 + \omega(\vartheta; \Delta\vartheta)] \bar{\kappa}_{\text{pair}}^{mn} - \bar{\kappa}_{\text{ind}}^{mn}. \quad (36)$$

For a consistent comparison with maps obtained by shear stacking, Sect. 5.1, we smooth the EMM with the same kernel as in Eq. (29),

$$\overline{\Delta\kappa}_{\text{emmm,K}}^{mn} = \frac{\sum_{n',m'=1}^{N_p, N_p} K(m - m', n - n') \overline{\Delta\kappa}_{\text{emmm}}^{m'n'}}{\sum_{n',m'=1}^{N_p, N_p} K(m - m', n - n')}, \quad (37)$$

we apply the same cropping, and we subtract the average of $\overline{\Delta\kappa}_{\text{emmm,K}}^{mn}$ from the cropped map.

5.4. Combining measurements

Our data consist of $i = 1 \dots n_f$ separate fields: four fields W1 to W4 for the CFHTLenS data and 64 fields for the synthetic data. Separated fields means here that we ignore contributions from galaxy pairs or triples where not all galaxies are inside the same field. For a combined measurement, we apply the estimators described in the foregoing sections for each field individually and then average them as described in the following. Our strategy for performing measurements of G3L with CFHTLenS data is improved in comparison to Simon et al. (2013). In that work, measurements in $n_f = 129$ individual pointings were performed and combined afterwards for a final result. Here, using the continuous fields W1-4, each consisting of many adjacent pointings, allows us to include also galaxy tuples with galaxies from different pointings. We find that this new strategy can enhance the overall S/N in the CFHTLenS maps moderately by 10-30 per cent, depending on the lens samples and their redshift binning.

For a combined estimate of GGL, we imagine the application of Eq. (32) to a merged catalogue of all fields where positions between any pair of galaxies from separate fields are larger than the considered range of ϑ . For this merged catalogue, let n_d^i and n_s^i be the number of lenses and sources inside field i , and $\bar{\gamma}_l^i + i\bar{\gamma}_x^i$ the estimator (32) for galaxies in field i only. We then split the sums over lens-source pairs in (32) for the merged catalogue into additive contributions from each field to obtain

$$\bar{\gamma}_l(\vartheta; \Delta\vartheta) + i\bar{\gamma}_x(\vartheta; \Delta\vartheta) = \frac{\sum_{i=1}^{n_f} W^i (\bar{\gamma}_l^i(\vartheta; \Delta\vartheta) + i\bar{\gamma}_x^i(\vartheta; \Delta\vartheta))}{\sum_{i=1}^{n_f} W^i} \quad (38)$$

with the field weights

$$W^i = \sum_{s,d=1}^{n_d^i, n_s^i} \Delta_{ds}^i(\vartheta; \Delta\vartheta) w_s^i \quad (39)$$

for the combined estimate. Here w_s^i are the statistical weights of sources s in field i , and the flag $\Delta_{ds}^i(\vartheta; \Delta\vartheta)$ applies to positions in field i only.

For the combined estimate of $1 + \omega$, we have to determine the count rates DD , DR , and RR in the merged catalogue. To this end, we cannot simply add the count rates of all individual fields. Instead we have to pay attention to the field variations of numbers n_d^i of observed galaxies and of unclustered random galaxies in the merged survey. For example, the number of random positions inside field i should depend on the effective area of the field. To quantify this, let p_i be the probability that a random position of unclustered galaxies is inside field i , and n_r is the total number of random points for all fields; the distribution of mocks in field i complies with the selection function in field i . Only if all fields have the same effective area (or selection function in general), we will find $p_i = p_j = 1/n_f$ for $i \neq j$. This, for example, is exactly the case for the 64 fields in our simulated data, and approximately for the 129 CFHTLenS pointings that make up the fields W1-4. For a measurement of the angular clustering of lenses in CFHTLenS, we combine the count rates inside the individual pointings, hence here $n_f = 129$; for all other correlation functions we perform measurements inside the large fields W1-4. Now, counting the total number of random-random pairs

in the merged catalogue we find

$$\frac{RR(\vartheta; \Delta\vartheta)}{n_r^2} = \frac{1}{n_r^2} \sum_{i=1}^{n_f} RR^i(\vartheta; \Delta\vartheta) = \sum_{i=1}^{n_f} p_i^2 \frac{RR^i(\vartheta; \Delta\vartheta)}{p_i^2 n_r^2} =: \sum_{i=1}^{n_f} p_i^2 rr^i(\vartheta; \Delta\vartheta), \quad (40)$$

where $rr^i := RR^i/(p_i^2 n_r^2)$ is the count rate RR^i in field i normalised with the total number $(p_i n_r)^2$ of random pairs in this field. Conveniently, the value of rr^i does not depend, on average, on the absolute number of mock positions that we actually in the individual measurement of field i . Therefore, for the combined result of normalised counts $rr = RR/n_r^2$, we take the average of all individual rr^i weighted with p_i^2 . Similarly, we obtain for the normalised count rate $dr = DR/(n_d n_r)$ of DR pairs in the merged catalogue

$$dr(\vartheta; \Delta\vartheta) := \sum_{i=1}^{n_f} \frac{p_i n_d^i}{n_d} \frac{DR^i(\vartheta; \Delta\vartheta)}{n_d^i p_i n_r} = \sum_{i=1}^{n_f} p_i f_i dr^i(\vartheta; \Delta\vartheta), \quad (41)$$

where $f_i = n_d^i/n_d$ is the fraction of galaxies in field i , and dr^i refers to the normalised rate in field i which, as before, does not depend on the number of mock positions used. Consequently, we compute the combined dr by taking a weighted sum of individual dr^i . The normalised count $dd = DD/n_d^2$ of DD pairs is

$$dd(\vartheta; \Delta\vartheta) := \sum_{i=1}^{n_f} f_i^2 dd^i(\vartheta; \Delta\vartheta). \quad (42)$$

In summary, we compute the count rates (dd^i, dr^i, rr^i) for each separate field i and then perform the previous weighted sums for the combined rates (dd, dr, rr). By means of the estimator (31), we then get

$$\omega(\vartheta; \Delta\vartheta) = \frac{dd(\vartheta; \Delta\vartheta)}{rr(\vartheta; \Delta\vartheta)} - 2 \frac{dr(\vartheta; \Delta\vartheta)}{rr(\vartheta; \Delta\vartheta)} + 1 \quad (43)$$

for the combined clustering amplitude of all fields.

With regard to combining measurements of the EMM (or PCM) from a set of n_f separate fields we do the following. We apply the estimator (27) with identical grid parameters to each field i for $\Delta\gamma_{mn}^i$ and the statistical weights W_{mn}^i . Therein, we constantly use the clustering amplitude $1 + \omega$ as estimated once from the merged catalogue and the measurement of the tangential shear $\bar{\gamma}_l^i$ in field i . This is consistent with the technique in Simon et al. (2008) but a slight variation compared to Simon et al. (2013) where $1 + \omega$ is measured for each CFHTLenS pointing individually. We then combine the measurements of the excess shear inside the fields into

$$\Delta\gamma_{mn} = \frac{\sum_{i=1}^{n_f} W_{mn}^i \Delta\gamma_{mn}^i}{\sum_{i=1}^{n_f} W_{mn}^i}. \quad (44)$$

Finally, we apply the smoothing (29) to the combined $\Delta\gamma_{mn}$ and perform the remaining steps in Sect. 5.1 for a combined map of the excess mass.

For a combined measurement of the EMM with the convergence-stack technique in Sect. 5.3, we just take the equally weighted average of all grids $\bar{\kappa}_{\text{emm}}^{mn}$ obtained from the individual $n_f = 64$ fields. An optimised weighting scheme is not necessary here because this simplistic approach already produces maps with negligible statistical noise for our simulated data.

5.5. Statistical errors

For an estimate of the statistical error in the CFHTLenS maps of the excess mass, we perform the jackknife technique (see e.g. Knight 1999). The basic idea is as follows. Let $G(d)$ be an estimator for some quantity G based on the complete data set d . In our case, $G(d)$ is our estimator for the smoothed EMM (or PCM) $\bar{\kappa}_{mn}^K$ at the grid pixel mn , and d comprises the merged catalogue of all separate fields. For the jackknife estimator, we split the complete data $d = d_1 \cup d_2 \cup \dots \cup d_{n_{\text{jn}}}$ into n_{jn} disjoint samples, and we compute a sample $\{G_{-i} : i = 1 \dots n_{\text{jn}}\}$ of estimates $G_{-i} := G(d \setminus d_i)$ based on d without the subset d_i . We define with

$$\sigma^2(G) = \frac{n_{\text{jn}} - 1}{n_{\text{jn}}} \sum_{i=1}^{n_{\text{jn}}} (G_{\circ} - G_{-i})^2, \quad (45)$$

for

$$G_{\circ} = \frac{1}{n_{\text{jn}}} \sum_{i=1}^{n_{\text{jn}}} G_{-i}, \quad (46)$$

the estimator of the jackknife error-variance of $G(d)$. For the following maps, we compute the jackknife error $\sigma(\bar{\kappa}_{mn}^K)$ for every pixel value $\bar{\kappa}_{mn}^K$ and quote $\bar{\kappa}_{mn}^K/\sigma(\bar{\kappa}_{mn}^K)$ for the S/N of a pixel value.

We expect that positional shot-noise and shape noise of the sources as well as cosmic variance are the dominating contributors of statistical noise in our measurement; see, for example, Kilbinger & Schneider (2005) for a discussion of statistical noise in related lensing correlation-functions. For the jackknife scheme, we remove individual pointings d_i from the merged catalogue; each CFHTLenS pointing has a square geometry and $1 \times 1 \text{ deg}^2$ area. Since these pointings are significantly larger than our EMM with typical angular scale of a few arcmin, we expect a sensible estimate for errors owing to cosmic variance at these scales (Shirasaki et al. 2017).

6. Results

In this section, we present maps of the excess mass for CFHTLenS lenses and for H15 galaxies in our synthetic data. We compute the maps in two versions for every selection of galaxy redshifts and angular separations on the sky: the excess-mass map (EMM) and the pair-convergence map (PCM). We consider pairs of lenses from the two angular separation bins $40'' \leq \theta_{12} < 60''$ ('close- θ ') and $60'' \leq \theta_{12} < 80''$ ('wide- θ '); and from the two redshift bins $0.2 \leq z_{\text{ph}} < 0.44$ ('low- z ') and $0.44 \leq z_{\text{ph}} < 0.6$ ('high- z '). We only report E-mode maps in this section; the corresponding B-mode maps can be found in the Appendix. The B-modes are consistent with a vanishing signal.

6.1. Code verification

For Fig. 4, we compare the reconstruction of the EMM with synthetic data for two different methods: shear stacking (Sect. 5.1) and convergence stacking (Sect. 5.3). Shown are only the reconstructions for close- θ galaxies in the high- z bin to save space. The relative deviations of maps for other samples, including the PCMs, are comparable to the single case shown here. The bottom panel employs for $\overline{\Delta\kappa}_{\text{em},2}$ the shear-stacking that we apply to the CFHTLenS data. The top panel displays the map $\overline{\Delta\kappa}_{\text{em},1}$ using direct convergence stacking. To reduce the noise in the maps for this comparison, we set the intrinsic shape noise of the sources to

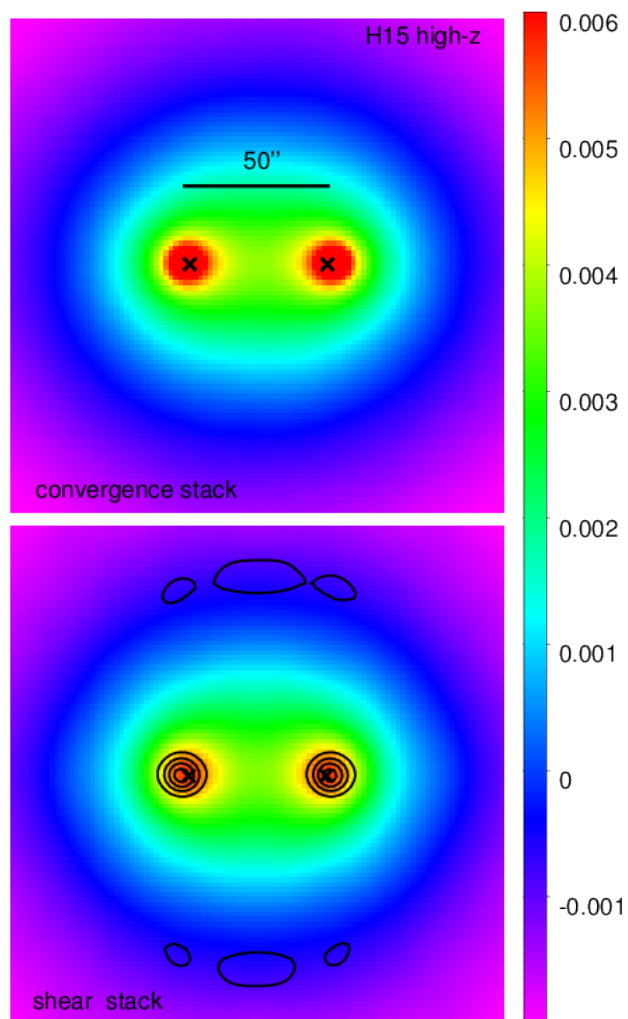


Fig. 4: Verification test with simulated data: A comparison of the E-mode EMM (intensity scale) obtained from the 1024 deg^2 mock data with two different method. Lens pairs are selected from the separation interval close- θ and redshift bin high- z ($\bar{z}_d \approx 0.52$). The lens positions inside the map are indicated by crosses. Shape and sampling noise of the sources are negligible here. *Top*: Explicit stacking of the convergence on a grid; only applied to the simulated data. *Bottom*: Reconstruction with a shear stack as applied to our CFHTLenS data. The contours show the relative difference $(\overline{\Delta\kappa}_{\text{em},2} - \overline{\Delta\kappa}_{\text{em},1})/\overline{\Delta\kappa}_{\text{em},1}$ between the two methods $\overline{\Delta\kappa}_{\text{em},1}$ (top) and $\overline{\Delta\kappa}_{\text{em},2}$ (bottom) in steps of 10%, 20%, etc. for regions where the signal magnitude is above 5×10^{-4} .

zero in the bottom panel; the number of sources in the shear catalogues is 2×10^4 for each of the 64 fields. Inside the panels, we indicate the lens positions p_1^d and p_2^d by black crosses. We overall find an excellent agreement for both approaches with relative differences usually around five per cent or less wherever the signal is larger than 5×10^{-4} . The differences grow larger, however, close the lens positions inside the map as indicated by the contours of $(\overline{\Delta\kappa}_{\text{em},2} - \overline{\Delta\kappa}_{\text{em},1})/\overline{\Delta\kappa}_{\text{em},1}$ with the error levels 10%, 20%, etc. Nevertheless, the errors are below 20% except within a couple of pixels separation from the lens positions. Presumably this error is owing to pixellation and binning of the GGL correlation function. The 10% error contours at the edges of the map are probably just numerical noise which becomes relevant for

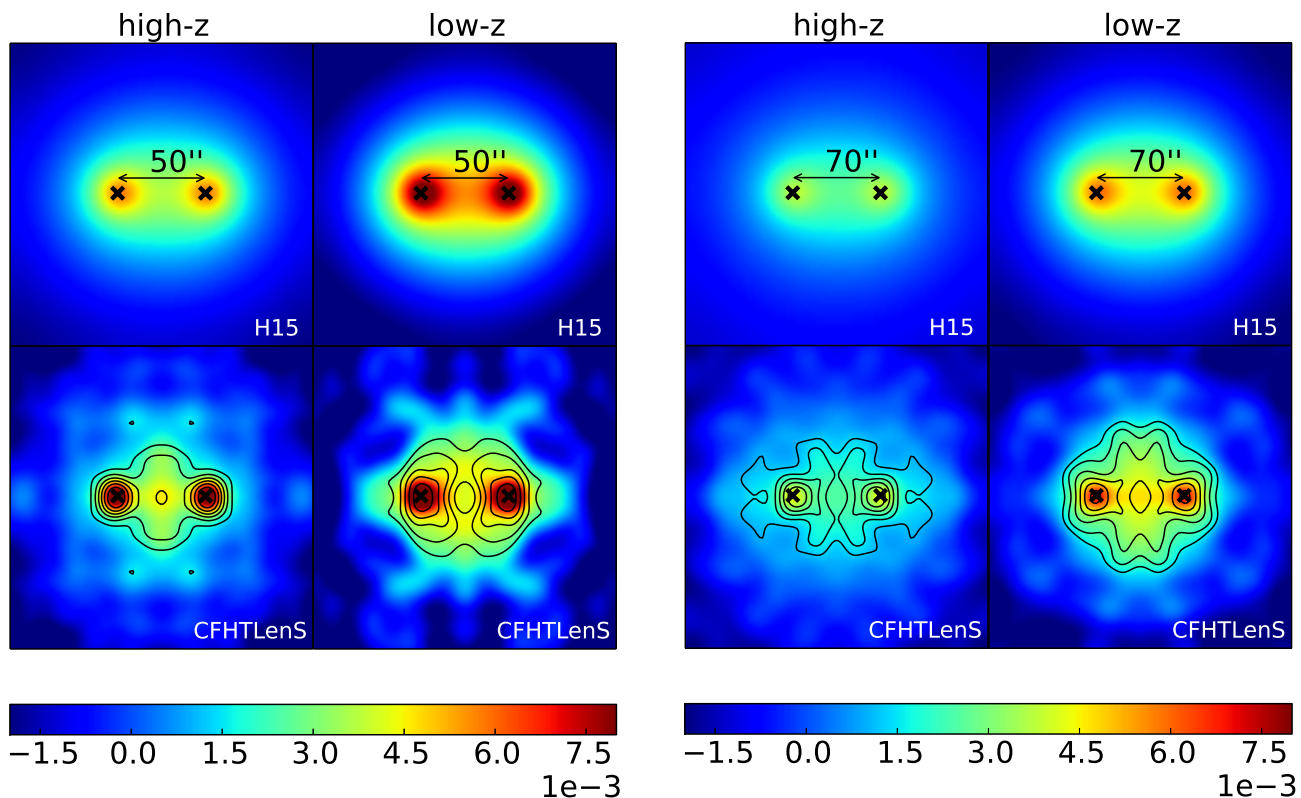


Fig. 5: Comparison of the E-mode EMM around H15 galaxy pairs (top rows; convergence stack) to measurements with CFHTLenS galaxies (bottom rows; shear stack). The left-hand columns correspond to high- z lens pairs, and the right-hand columns correspond to low- z pairs. The CFHTLenS contours at the bottom follow significance levels starting from 3σ in steps of 1σ (outer to inner contours). *Left*: Maps for the angular bin close- θ . The projected lens-lens distance is $\approx 174 h^{-1}$ kpc for low- z and $\approx 220 h^{-1}$ kpc for high- z . *Right*: Maps for the angular bin wide- θ . The projected lens-lens distance is $\approx 244 h^{-1}$ kpc for low- z and $\approx 308 h^{-1}$ kpc for high- z .

values of $\overline{\Delta\kappa_{\text{emm},1}}$ that are close to zero; the convergence stacking randomly picks a separation to an imaginary lens to subtract second-order correlations from the map. We reiterate that shear stacking is insensitive to constant offsets in κ so that this level of agreement here is only valid for a consistent definition of κ_0 .

6.2. Excess-mass maps

Figure 5 shows the estimated EMM for the separation bin close- θ as measured in CFHTLenS (bottom panels) in comparison to the H15 predictions (top panels). The samples are split in redshift with high- z galaxies in the left columns and low- z in the right columns. The mean redshifts and angular separations of lenses inside the bins correspond to projected distances between $\approx 170 - 300 h^{-1}$ kpc. The measurements in CFHTLenS are subject to strong statistical noise due to positional shot-noise and shape noise of the sources. Based on jackknife resampling of the data, the contour lines show a 3σ significance for the outer contour and a stepwise increase by 1σ towards the inner contours. Clearly, we find a significant detection of excess mass only in the central part of the map close and between the lens positions ($3\sigma - 6\sigma$). In comparison, cosmic variance and shot noise by lenses are the only noise components present in the top panels with the synthetic data. Similar to the model predictions for the G3L aperture-statistics in S+17, statistical noise is neg-

ligible here so that we do not show S/N contours. Apart from noise in the CFHTLenS maps, we find a good agreement with the predictions for H15 galaxies: a strong concentration of excess mass close to the lens positions and a drop of the signal by about $\Delta\kappa = 4 \times 10^{-3}$ from the centre to the outer regions of the maps. This drop corresponds to a change in the excess surface-mass density of $\Delta\kappa \times \overline{\Sigma}_{\text{crit}} \approx 17 h M_{\odot} \text{pc}^{-2}$ for the fiducial value of $\overline{\Sigma}_{\text{crit}}$ in Eq. (19). We also observe a tentative indication of a morphological difference between CFHTLenS data and the SAM for lens pairs with projected distance of $\approx 220 - 300 h^{-1}$ kpc, that is for the samples close- θ /high- z and wide- θ /low- z : the excess mass has a bulge-like distribution in vertical direction which is absent in the simulations; the distribution in the simulated maps is elongated along the line connecting the lenses inside the map. This bulge in CFHTLenS is more pronounced in the following PCMs.

6.3. Pair-convergence maps

For Fig. 6, we plot the distribution of pair convergence for our galaxy samples. Again, we have the H15 model predictions in the top panel and the corresponding CFHTLenS measurements in the bottom panels; the samples are split in redshift and in angular separation of the lenses as indicated for the panels. We point out in Sect. 3.2 that the distribution of excess mass in these PCMs is less affected by chance pairs. However, the then miss-

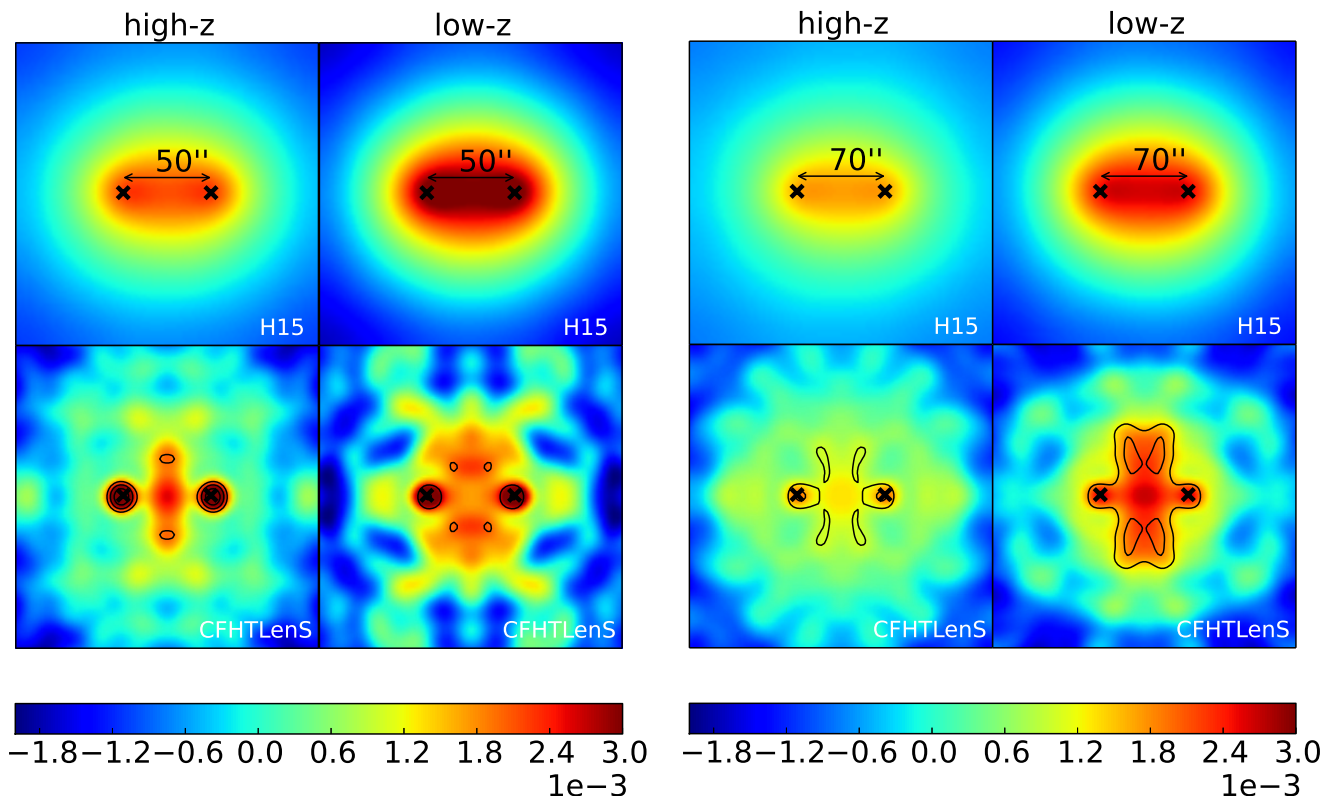


Fig. 6: Similar to Fig. 5 but now for the E-mode of the PCMs.

ing additional contribution by CP in the EMM has the effect that the significance levels in the PCMs are lower than in the EMMs; the overall amplitude of the signal is also diminished by the fraction of CP in the lens sample. For instance, the significance of the PCM signal between lenses is now just below 3σ for close- θ . In addition, the signal drop $\Delta\kappa$ from the map centre to the outer regions is typically smaller for the PCM, roughly by a factor of two, namely $2 \times 10^{-3} \bar{\Sigma}_{\text{crit}} \approx 8 h M_{\odot} \text{pc}^{-2}$. This is a lower limit to the actual drop in the excess surface mass-density of true lens pairs since this value scales with the fraction p_{tp} of TP; see Eq. (24).

Moreover, in the PCM the difference between the signals at the lens positions (crosses) and the centre of the maps is smaller than for the EMM. For the PCMs of the mock data, we have no pronounced peak in excess mass at the lens positions but just a diffuse halo in which the lenses are embedded. Although this is similar for the CFHTLenS wide- θ samples (right figure) this is not the case for the close- θ samples (left figure). This may in parts be related to the 10-20 per cent inaccuracy of the shear stacking that we find within a few pixels of the lens positions; see Sect. 6.1.

More prominently and different to the SAM prediction, there is a bulge in the distribution of the excess mass between the galaxies; see in particular the ‘gummy-bear’ like shape for the wide- θ lenses in the low- z bin. To enhance the significance of this feature in the redshift bins of the PCMs, we combine all shear stacks of low- z and high- z for the same angular separations of lenses in Fig. 7. We again estimate significance in the combined PCMs by applying the jackknifing technique in Sect. 5.5 with $n_{\text{jn}} = 129$ jackknife samples; for each sample we re-

move both the low- z and the high- z bin of the same CFHTLenS pointing. The redshift-combined PCMs exhibit the bulges with a significance of 3σ for close- θ (left panel) and 4σ for wide- θ (right panel). This may be a tentative indication of a disagreement between the H15 prediction and CFHTLenS galaxies. We discuss our results in the following.

7. Discussion

Our results for the EMM in the Fig. 5 show a clear $3\sigma - 6\sigma$ detection of the correlated excess-mass within the inner few $100 h^{-1} \text{kpc}$ around CFHTLenS galaxy-pairs, and the signal has the expected qualitative behaviour for changes in galaxy separation and redshift. As to the galaxy sample, we select galaxies with stellar masses between $\sim 10^9 - 10^{11} M_{\odot}$, projected mutual distances of about $170 - 300 h^{-1} \text{kpc}$, and redshifts $z_{\text{d}} \lesssim 0.6$. By rejecting stellar masses below $3 \times 10^9 M_{\odot}$ we obtain an approximately volume-limited sample despite the flux limit $i' \leq 22.5$. Our stellar-mass range comprises galaxies around the characteristic mass $M_* \approx 5 \times 10^{10} M_{\odot}$ of the stellar-mass function (Wright et al. 2017, and references therein). Compared to the previous G3L measurements in S+13, these new measurements include lens-lens-source triplets across adjacent CFHTLenS pointings and hence improve the S/N in the EMM estimators by up to 20 – 30%. For these measurements, the B-mode EMMs in the top panel of Fig. A.2 (Appendix) are indicators of systematic errors. To enhance the significance of the indicators, we also combine the B-mode maps for low- z and high- z in this figure. The consistency of the indicators with random noise supports that systematic errors are negligible inside the maps, at

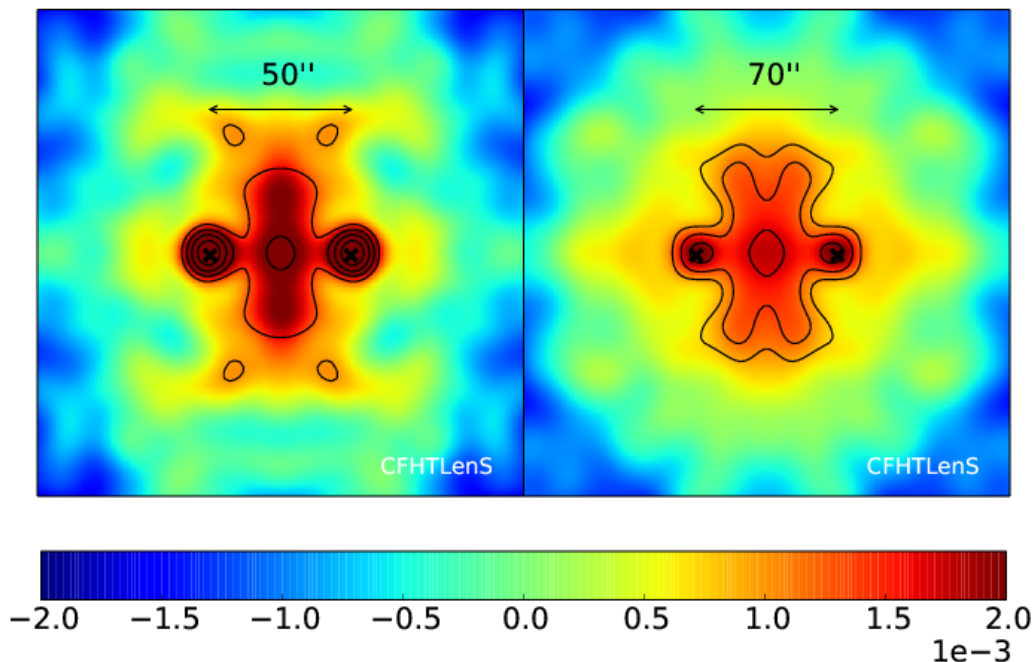


Fig. 7: Combination of the CFHTLenS PCMs, as shown in the Fig. 6, for the angular separations close- θ (left panel) and wide- θ (right panel). The maps combine the shear stacks of the redshift bins low- z and high- z to increase the S/N. The contours indicate iso-levels of detection significance from 3σ to 6σ in 1σ steps from the outer to inner contours. Clearly visible is the bulge in the distribution of excess mass between the lenses.

least those that can be detected by B-modes. Moreover, our E-mode signal for the EMM decreases with lens separation at a fixed redshift, compare close- θ to wide- θ for the same redshift bin, and it decreases with redshift as seen by a comparison of low- z and high- z for the same angular bin. Both is broadly expected: the same angular separation of galaxies on the sky at increasing redshift corresponds to larger projected distances and the three-point correlation function of the matter density field decreases with physical scale; galaxies are essentially tracers of the matter density and therefore their three-point correlations have a similar qualitative behaviour. The EMM signal also varies with the lensing efficiency as expressed by Eq. (19). The relative decrease of $\bar{\Sigma}_{\text{crit}}$ between low- z ($\bar{z}_d = 0.35$) and high- z ($\bar{z}_d = 0.52$) is approximately 15% and thus contributes to a signal decrease. An additional signal decrease towards higher redshift may be given by gravitational growth of structure which amplifies the non-Gaussianity of the density fields with time.

We have introduced the pair convergence as alternative measure of the excess mass to suppress the contamination by chance pairs in the correlation statistics, and we detect it with a significance of $3\sigma - 4\sigma$ for our CFHTLenS lenses. Our mapping technique of the excess mass stacks shear around galaxy pairs within a given separation interval on the sky. However, a fraction $p_{\text{cp}} := 1 - p_{\text{tp}}$ of pairs is well separated in physical distance so that they can be considered statistically independent for practical purposes: they dilute the correlation signal and, importantly, in a EMM add extra excess-convergence centred on the lens po-

sitions inside the map, as described in Sect. 3.2. The latter is clearly visible at the crosses in the verification maps of Fig. 5, for instance. It may be desired to remove this extra convergence by rejecting chance pairs in the stack. However, the selection of galaxy pairs with distances well below the large-scale coherence length $100 h^{-1}$ Mpc or redshift differences less than about $\Delta z \sim 0.03$ is difficult owing to the errors $\sigma(z) \approx 0.04$ of the photometric-redshift estimators. Therefore, we have defined by Eq. (17) a slightly modified statistic PCM which is less affected by chance pairs. Although a fraction p_{cp} of chance pairs still dilutes the overall signal in the map, the PCM no longer adds extra convergence at the lens positions. This is visible when comparing the top left panels of the simulated EMM in Fig. 5 and the simulated PCM in Fig. 6. As expressed by Eq. (24), for an average surface-mass density $\bar{\Sigma}_{\text{crit}}$ of the lens and source samples the PCM has a simpler interpretation than the EMM: it is the stacked surface mass-density around true pairs in excess of the average surface mass-density around two single lenses, normalised with the surface-mass density $p_{\text{tp}}^{-1} \times \bar{\Sigma}_{\text{crit}}$. On the other hand, the EMM may be mathematically preferable because it is only a function of the matter-galaxy bispectrum and thus exactly vanishes for Gaussian density fields (Schneider & Watts 2005). The detection significance of the PCM, Fig. 6, is lower than for the corresponding EMM, Fig. 5, presumably because of the removal of contributions from chance pairs while retaining a comparable noise level as reflected by the B-mode maps in Fig. A.2 that

are similar for the EMMs and PCMs. To increase the S/N in the PCM to $3\sigma - 4\sigma$ in the vicinity of the galaxy positions, we combine the shear stacks of low- z and high- z for same angular bins in Fig. 7.

As expected from the recent work by S+17, there is a good agreement between the H15 predictions for the EMM and our measurements with CFHTLenS data although we find weak evidence for morphological differences to SAMs in the PCMs. S+17 measured, among other things, the aperture statistics $\langle N^2 M_{\text{ap}} \rangle(\theta_{\text{ap}})$ for angular scales θ_{ap} between one arcmin and 10 arcmin for the galaxy samples sm1 to sm6 in the low- z and high- z redshift bin and compare these to H15 predictions. The good match between observation and theory of all stellar-mass samples is underlined by $\chi^2/\text{dof} = 1.34(2.08)$ for $\text{dof} = 48$ degrees of freedom in the low- z (high- z) bin, reported in Table 6 of S+17. Since these aperture statistics are essentially an integral over \mathcal{G} or EMMs with varying lens-lens separations and θ_{ap} -dependent integral kernels, we expect that the H15 EMMs also agree well with the measurements despite probing somewhat smaller angular scales (Schneider & Watts 2005). Indeed the H15 distribution of excess mass and its overall amplitude is consistent with CFHTLenS, cf. the top and bottom panels in the Fig. 5. With regard to possible differences between the H15 prediction and CFHTLenS, we notice the bulge of excess mass in vertical direction at the centre of the EMMs; see in particular lens pairs in the low- z and wide- θ bin in Fig. 5 and also the EMM of early-type galaxies in Figure 8 of S+13 based on the same shear data. This feature becomes more pronounced, albeit less significant, in the PCMs of the Fig. 6, but is clearly visible in the combined maps of Fig. 7. By comparison the PCMs of H15 in the top panels of Fig. 6 do not exhibit the bulge. The same is the case for the three other SAMs discussed in S+17, as shown in Saghiha (2017). From the PCMs in Fig. 7, we estimate that the significance of the bulge is at most 4σ . This morphological feature may be a random fluke that is produced by correlated noise in the maps. For example, the B-mode maps in Fig. A.2 are basically realisations of correlated noise.

We have taken precautions to suppress spurious signals in the maps owing to intrinsic alignments of sources, and we have performed basic tests to rule out that the bulge feature is not a trivial systematic error. Correlations of intrinsic source ellipticities with the matter density around lens pairs can add signal to our maps of the excess mass. Although this effect is not well studied at this point, S+13 argue that the alignment signal can be suppressed for G3L by separating lens and source galaxies in redshift which has been done for our galaxy samples by using photometric redshifts. This separation is not perfect but the overlap of the distributions is small: approximately 4% for low- z and 12% for high- z (S+13). In particular, the bulge is still visible for low- z and wide- θ lens pairs in Fig. 6 despite the small 4% overlap for low- z . Therefore, the bulge is probably unrelated to intrinsic alignments. Furthermore, numerical artefacts in the computer code that produce a bulge feature are also unlikely as can be seen by the verification test in Fig. 4. Here systematic errors are present close to the lens positions only. However, masking of data is not included in the verification test. But it is not plausible why mask-related systematic errors should have a preferred map direction unless the orientation of galaxy pairs at $z_d \gtrsim 0.2$ is correlated with the orientation of mask features; masking is mainly produced by satellite tracks, stars, instrumental CCD effects, cosmic rays, or low-redshift galaxies (Erben et al. 2013). As another possible systematic effect, we test if blending of galaxy images could bias the shear estimates of CFHTLenS sources and affect the excess maps (Miller et al. 2013). For the test, we have pro-

duced new maps with same binning parameters as in Fig. 5 by rejecting sources within nine arcsec of a lens galaxy for the shear stack. We find no significant difference to the maps without rejection, and, in particular, the bulge feature persists (not shown to save space). Finally, we stack the PCM shear-patterns of all angular and redshift bins in Fig. 6 to investigate a possible residual pattern in the B-modes that is correlated with the bulge feature. We overlay the B-mode signal as black contours in Fig. A.3 on top of the combined E-mode PCM. The merged stacks of all lenses clearly show the bulge at the centre; the B-mode amplitude is typically below 5×10^{-4} near the bulge and thus small compared to the E-mode signal; see the intensity scale. However, the B-mode signal is correlated with the bulge: it extends to larger separations in vertical direction at the positions of the lenses (crosses) compared to its vertical extension at the bulge location. This might be a coincidence or an indication of a systematic effect for the bulge appearance. A clear interpretation of an alignment between a residual B-mode signal and the E-mode bulge is difficult, however, since we lack a model for systematic errors here that connects both.

On the speculative side, if the bulge in the distribution of excess mass is indeed a physical effect it could point to missing elements in the dark-matter simulation or the SAM galaxy model (or the similar SAMs in S+17) used for this study. One conceivable element might be the extra lensing signal by the intra-cluster medium (ICM) that constitutes 10 – 15% of the mass of matter halos in galaxy clusters. On the one hand, if the ICM distribution is aligned with the distribution of dark matter (DM), there will be no qualitative change in the distribution of excess mass because additional gravitational lensing by the ICM only rescales the dominating DM signal. On the other hand, a misalignment between the ICM and DM distribution might produce a weak bulge feature if the ICM density is increased perpendicular to the lens-lens axis. This could be tested with cosmological simulations that include baryons, or analytically with a halo model that includes misaligned mass-distributions (e.g. Cooray & Sheth 2002). Similarly, we could imagine a bulge feature by a statistical misalignment between the orientation of lens pairs and the orientation of their parent halo. As an extreme example, one might consider a distribution of galaxies distributed in the equatorial plane of a prolate halo. Stacking the surface matter-density of the halo around pairs of these galaxies would result in an elongated excess signal perpendicular to the orientation of lens pairs. This too could be tested with simulations or a halo model by populating non-spherical dark-matter halos with a misaligned galaxy distribution.

By selecting galaxy pairs with projected separations of around $250 h^{-1}$ kpc our analysis probes the matter environment of pairs inside galaxy groups and clusters. While this regime is of particular interest for galaxy models, such as H15, in future applications this probe can also be utilised to analyse the filamentary large-scale distribution of matter around physical pairs. To this end, we would map the pair convergence around luminous red galaxies at $\sim 10 h^{-1}$ Mpc separation, in a way that is similar to Epps & Hudson (2017) and Clampitt et al. (2016).

Acknowledgements

This work has been supported by the Deutsche Forschungsgemeinschaft through the project SI 1769/1-1 and through the Collaborative Research Center TR33 ‘The Dark Universe’. Patrick Simon also acknowledges support from the German Federal Ministry for Economic Affairs and Energy (BMWi) provided via DLR under project no. 50QE1103. Stefan Hilbert acknowledges

support by the DFG cluster of excellence ‘Origin and Structure of the Universe’ (www.universe-cluster.de).

References

- Aihara, H., Arimoto, N., Armstrong, R., et al. 2017, *arXiv*: 1704.05858
- Bartelmann, M. & Schneider, P. 2001, *Phys. Rep.*, 340, 291
- Becker, M. R., Troxel, M. A., MacCrann, N., et al. 2016, *Phys. Rev. D*, 94, 022002
- Benitez, N. 2000, *ApJ*, 536, 571
- Bridle, S., Balan, S. T., Bethge, M., et al. 2010, *MNRAS*, 405, 2044
- Buddendiek, A., Schneider, P., Hildebrandt, H., et al. 2016, *MNRAS*, 456, 3886
- Chabrier, G. 2003, *PASP*, 115, 763
- Choi, A., Tyson, J. A., Morrison, C. B., et al. 2012, *ApJ*, 759, 101
- Clampitt, J., Miyatake, H., Jain, B., & Takada, M. 2016, *MNRAS*, 457, 2391
- Clampitt, J., Sánchez, C., Kwan, J., et al. 2017, *MNRAS*, 465, 4204
- Cooray, A. & Sheth, R. 2002, *Phys. Rep.*, 372, 1
- Coupon, J., Arnouts, S., van Waerbeke, L., et al. 2015, *MNRAS*, 449, 1352
- Epps, S. D. & Hudson, M. J. 2017, *MNRAS*, 468, 2605
- Erben, T., Hildebrandt, H., Miller, L., et al. 2013, *MNRAS*, 433, 2545
- Gillis, B. R., Hudson, M. J., Erben, T., et al. 2013, *MNRAS*, 431, 1439
- Henriques, B. M. B., White, S. D. M., Thomas, P. A., et al. 2015, *MNRAS*, 451, 2663
- Heymans, C., Van Waerbeke, L., Bacon, D., et al. 2006, *MNRAS*, 368, 1323
- Heymans, C., Van Waerbeke, L., Miller, L., et al. 2012, *MNRAS*, 427, 146
- Hilbert, S., Hartlap, J., White, S. D. M., & Schneider, P. 2009, *A&A*, 499, 31
- Hildebrandt, H., Choi, A., Heymans, C., et al. 2016, *MNRAS*, 463, 635
- Hildebrandt, H., Erben, T., Kuijken, K., et al. 2012, *MNRAS*, 421, 2355
- Hoekstra, H., van Waerbeke, L., Gladders, M. D., Mellier, Y., & Yee, H. K. C. 2002, *ApJ*, 577, 604
- Johnston, D. E. 2006, *MNRAS*, 367, 1222
- Kaiser, N. 1995, *ApJ*, 439, L1
- Kaiser, N. & Squires, G. 1993, *ApJ*, 404, 441
- Kilbinger, M. & Schneider, P. 2005, *A&A*, 442, 69
- Kitching, T. D., Balan, S. T., Bridle, S., et al. 2012, *MNRAS*, 423, 3163
- Knight, K. 1999, *Mathematical Statistics*, Chapman & Hall/CRC Texts in Statistical Science (CRC Press)
- Kuijken, K., Heymans, C., Hildebrandt, H., et al. 2015, *MNRAS*, 454, 3500
- Landy, S. D. & Szalay, A. S. 1993, *ApJ*, 412, 64
- Mandelbaum, R., Hirata, C. M., Broderick, T., Seljak, U., & Brinkmann, J. 2006a, *MNRAS*, 370, 1008
- Mandelbaum, R., Rowe, B., Bosch, J., et al. 2014, *ApJS*, 212, 5
- Mandelbaum, R., Seljak, U., Cool, R. J., et al. 2006b, *MNRAS*, 372, 758
- Mandelbaum, R., Seljak, U., Kauffmann, G., Hirata, C. M., & Brinkmann, J. 2006c, *MNRAS*, 368, 715
- Massey, R., Heymans, C., Bergé, J., et al. 2007, *MNRAS*, 376, 13
- Miller, L., Heymans, C., Kitching, T. D., et al. 2013, *MNRAS*, 429, 2858
- Mo, H., van den Bosch, F. C., & White, S. 2010, *Galaxy Formation and Evolution* (Cambridge University Press)
- Peebles, P. J. E. 1980, *The large-scale structure of the universe* (Princeton University Press)
- Pen, U.-L., Lu, T., van Waerbeke, L., & Mellier, Y. 2003, *MNRAS*, 346, 994
- Planck Collaboration, Ade, P. A. R., Aghanim, N., et al. 2016, *A&A*, 594, A13
- Prat, J., Sánchez, C., Miquel, R., et al. 2016, *arXiv*: 1609.08167
- Saghiha, H. 2017, PhD thesis, AIfA - Argelander-Institut für Astronomie, Rheinische Friedrich-Wilhelms Universität Bonn, Germany, <http://hss.ulb.uni-bonn.de/2017/4643/4643.htm>
- Saghiha, H., Hilbert, S., Schneider, P., & Simon, P. 2012, *A&A*, 547, A77
- Saghiha, H., Simon, P., Schneider, P., & Hilbert, S. 2017, *A&A*, 601, A98
- Schneider, P. 2003, *A&A*, 408, 829
- Schneider, P., Kochanek, C., & Wambsganss, J. 2006, *Gravitational lensing: strong, weak and micro*, Saas-Fee Advanced Course: Swiss Society for Astrophysics and Astronomy (Springer)
- Schneider, P. & Watts, P. 2005, *A&A*, 432, 783
- Schrabback, T., Hilbert, S., Hoekstra, H., et al. 2015, *MNRAS*, 454, 1432
- Shirasaki, M., Takada, M., Miyatake, H., et al. 2017, *MNRAS*, 470, 3476
- Simon, P. 2012, *A&A*, 543, A2
- Simon, P., Erben, T., Schneider, P., et al. 2013, *MNRAS*, 430, 2476
- Simon, P. & Schneider, P. 2017, *A&A*, 604, A109
- Simon, P., Schneider, P., & Kübler, D. 2012, *A&A*, 548, A102
- Simon, P., Watts, P., Schneider, P., et al. 2008, *A&A*, 479, 655
- Springel, V., White, S. D. M., Jenkins, A., et al. 2005, *Nature*, 435, 629
- van Uitert, E., Hoekstra, H., Joachimi, B., et al. 2017, *MNRAS*, 467, 4131
- Velander, M., van Uitert, E., Hoekstra, H., et al. 2014, *MNRAS*, 437, 2111
- Viola, M., Cacciato, M., Brouwer, M., et al. 2015, *MNRAS*, 452, 3529
- Watts, P. & Schneider, P. 2005, in *IAU Symposium*, Vol. 225, *Gravitational Lensing Impact on Cosmology*, ed. Y. Mellier & G. Meylan, 243–248
- Wittman, D., Dell’Antonio, I. P., Hughes, J. P., et al. 2006, *ApJ*, 643, 128
- Wright, A. H., Robotham, A. S. G., Driver, S. P., et al. 2017, *MNRAS*, 470, 283

Appendix A: Additional figures

As additional characterisation of the population of lens galaxies in our analysis of the excess mass, we plot in Fig. A.1 their distribution of absolute rest-frame magnitudes or colours for (photometric) redshifts z_B between 0.2 and 0.6. Moreover, the Figures A.2 and A.3 are maps of the B-mode signal of the excess mass which are a diagnostic for systematic errors in the correlation signal.

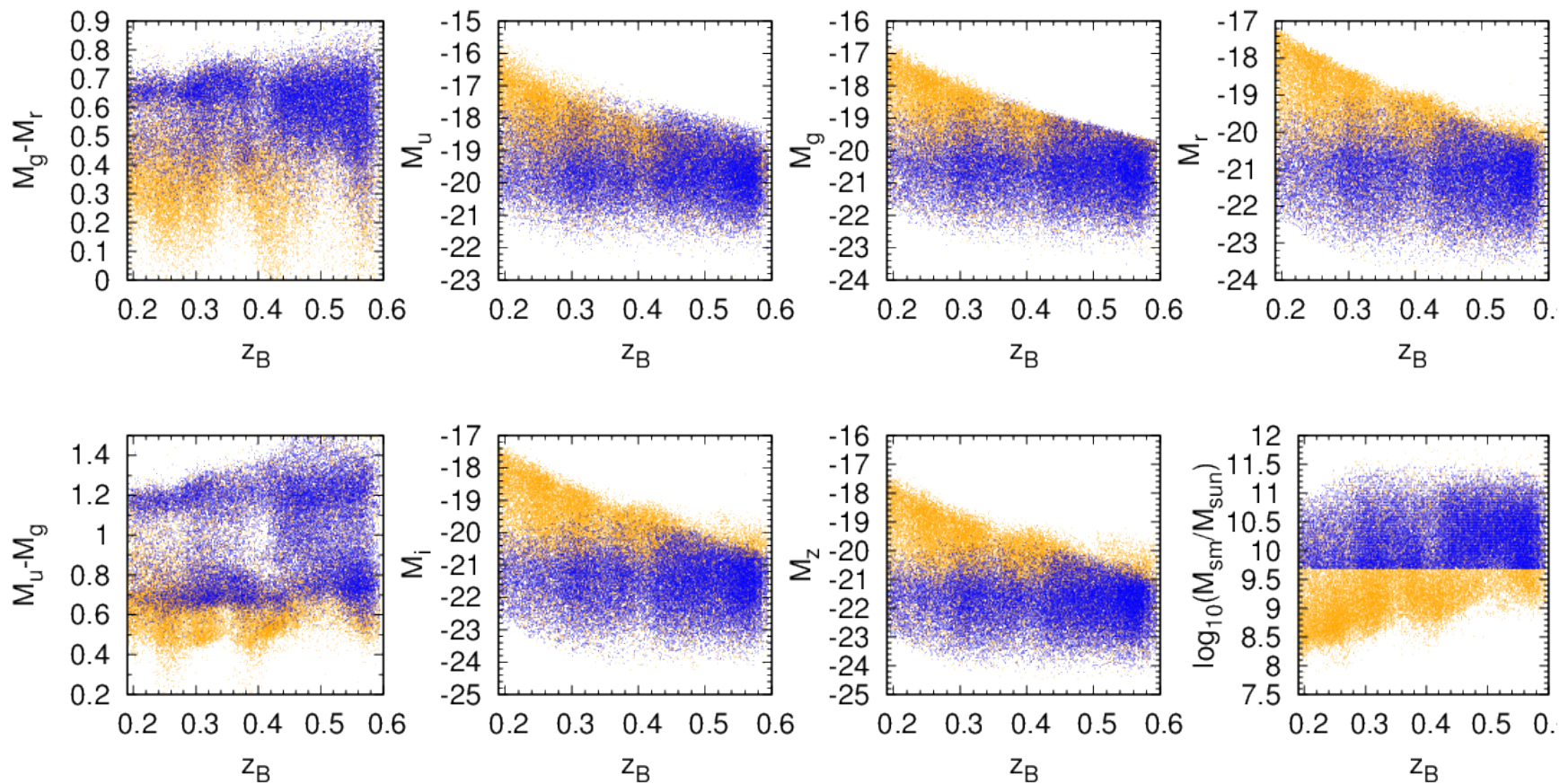


Fig. A.1: Properties of the targeted sample of lens galaxies in the G3L analysis. Shown are scatter plots of absolute rest-frame $u^*g'r'i'z'$ -magnitudes, colours, and stellar masses versus the photometric redshift z_B (BPZ) of the CFHTLenS galaxies with flux limit $i' < 22.5$ in the stellar-mass interval $5 \times 10^9 \leq M_{sm} < 3.2 \times 10^{11} M_{\odot}$ (blue dots). The brighter orange dots show the scatter for lenses for all stellar masses which are clearly flux limited at higher redshifts z_B . The data points are from galaxies in the field W1 only; other fields look similar.

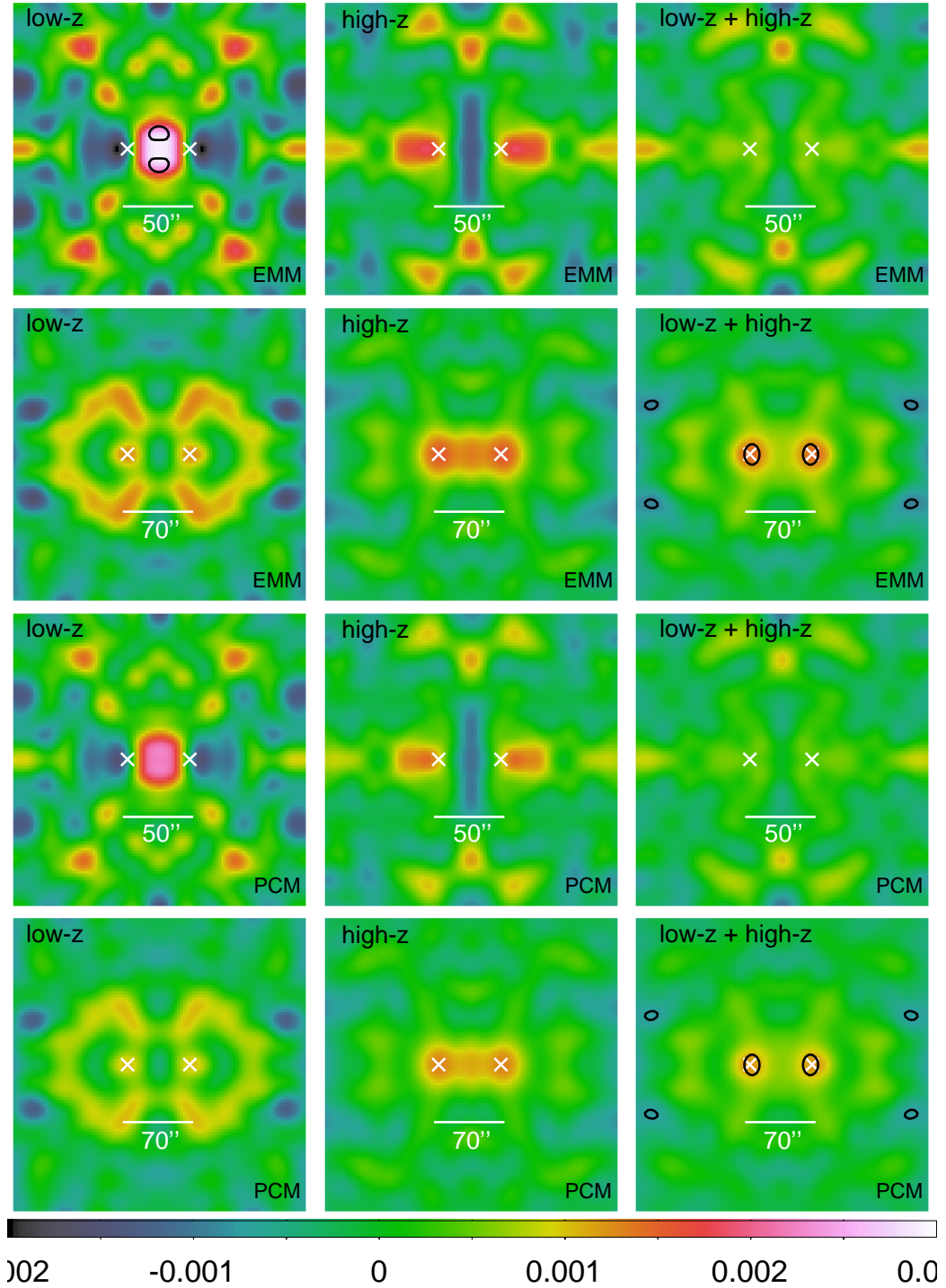


Fig. A.2: B-mode maps of the excess mass around CFHTLenS galaxy pairs for the EMM (top panels) and the PCM (bottom panels). The angular scale and redshift selections are indicated inside the panels. The crosses show the lens positions inside the map. The contours indicate regions with significance greater or equal 3σ .

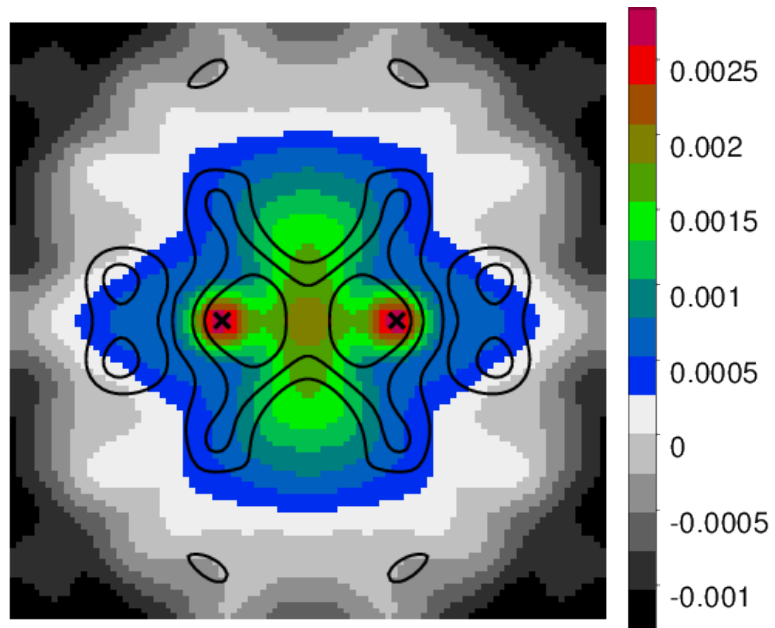


Fig. A.3: The average of all PCMs in Fig. 6 and the corresponding B-mode maps by combining all shear stacks used for that figure. The E-mode is shown here as intensity scale, the B-mode is shown as overlay of iso-contours for the levels 2×10^{-4} , 4×10^{-4} , and 6×10^{-4} .